

**Characterizing a novel human induced pluripotent stem cell-derived neuronal model of
Smith-Magenis syndrome**

Yoobin Cho

Integrated Program in Neuroscience

McGill University, Montréal, Québec, Canada

December 2023



A thesis submitted to McGill University in partial fulfillment of the requirements of the degree
of Master of Science

© Yoobin Cho, 2023

Dedication

I dedicate this work to my loving family who have endlessly supported me in all my endeavours, and to the friends I made on this journey, who shared with me their relentless drive, wisdom, and curiosity.

Table of Contents

Dedication	2
Abstract	5
Résumé	6
Acknowledgments	7
Contribution to Original Knowledge	8
Contribution of Authors	9
List of Tables and Figures	10
List of Abbreviations	11
1. Introduction	13
1.1 Human neurodevelopment and neurodevelopmental disorders	13
1.2 Human iPSC-derived models of ASD	15
1.3 Smith-Magenis syndrome	18
1.4 Retinoic Acid-Induced 1	19
1.5 Rodent and cellular models of SMS	20
1.6 Project overview	22
2. Materials and Methods	23
2.1 Subjects and hiPSC lines	23
2.2 Cell Culture	23
2.3 Quality control of hiPSCs and derived cells	24
2.4 RNA extraction and quantitative PCR	25
2.5 Immunocytochemistry	25

2.6 Data acquisition from immunofluorescence images	26
2.7 Neuronal morphometric analyses	27
2.8 Dendritic spine morphometric analyses.....	28
2.9 Statistical analyses	28
3. Results	30
4. Discussion	38
Conclusion and Summary.....	45
References	46
Figures	53

Abstract

Smith-Magenis syndrome (SMS) is a currently incurable neurodevelopmental disorder characterized by autistic features, epilepsy, sleep disturbances, and developmental delay. Patients have genomic deletions of varying sizes on chromosome 17 locus p11.2, which includes *Retinoic Acid-Induced 1 (RAI1)*, a gene encoding a transcriptional regulator crucial for neurodevelopment. While evidence in mice found that *Rai1* loss in excitatory neurons leads to SMS-like phenotypes, it remains difficult to recapitulate the complex neuropathology of SMS in animal models. Furthermore, little is known about the cellular mechanisms affected by 17p11.2 deletions in the human brain. By investigating human induced pluripotent stem cell (hiPSC)-derived neural progenitor cells (NPCs) and neurons, this project contributes to elucidating the role of *RAI1*-encompassing 17p11.2 in human neurodevelopment and disease. My thesis describes how SMS patient and healthy control somatic cell-derived hiPSCs were differentiated into NPCs and forebrain neurons. It identifies the cellular processes and morphological characteristics affected by 17p11.2 deletions in this model, providing insight into how genes in this region may play a role in both normal neurodevelopment and disease.

Résumé

Le syndrome de Smith-Magenis (SMS) est un trouble neurodéveloppemental sans traitement disponible caractérisé par des traits autistiques, de l'épilepsie, des perturbations du sommeil et un retard de développement. Les patients présentent des délétions génomiques de tailles variées sur le locus p11.2 du chromosome 17, incluant *Retinoic Acid-Induced 1 (RAI1)*, un gène codant pour un régulateur transcriptionnel crucial pour le neurodéveloppement. Bien que des preuves chez la souris aient montré que la perte de *Rai1* dans les neurones excitatoires induit des phénotypes similaires au SMS, il reste difficile de reproduire la neuropathologie complexes du SMS dans des modèles animaux. De plus, peu d'informations sont disponibles sur les mécanismes cellulaires affectés par les délétions 17p11.2 dans le cerveau humain. En étudiant les cellules progénitrices neurales (NPC) et les neurones dérivés de cellules souches pluripotentes induites humaines (hiPSC), ce projet contribue à élucider le rôle de la délétion 17p11.2 englobant RAI1 dans le neurodéveloppement humain et la maladie. Ma thèse décrit comment les hiPSC dérivées de cellules somatiques de patients atteints du SMS et de sujets témoins en bonne santé ont été différenciées en NPC et en neurones du cerveau antérieur. Elle identifie les processus cellulaires et les caractéristiques morphologiques affectés par les délétions 17p11.2 dans ce modèle, offrant ainsi un aperçu de la manière dont les gènes de cette région pourraient jouer un rôle à la fois dans le neurodéveloppement normal et au maladie.

Acknowledgements

This project would not have been possible without Dr. Wei-Hsiang Huang. I am very grateful to have been under the supervision of such a brilliant mind, who has kept me challenged yet inspired to persevere in my scientific endeavours. I would like to thank my IPN mentor, Dr. Aparna Suvrathan, for providing valuable advice throughout my program milestones. My advisory committee members, Dr. Thomas Durcan and Dr. Carl Ernst, provided insightful feedback to drive my project forward – your provision of stem cell lines and shared expertise on iPSC work are greatly appreciated. I also thank the CanNRT for funding my work.

I have been very fortunate to be surrounded by such hard-working and supportive individuals during my time at the lab. I would first like to thank Dr. Yu-Ju Lee for collaborating with me on this project, and for helping me build my wet-lab skills from the ground up. I would also like to thank Dr. Ya-Ting Chang for teaching me the secrets of immunostaining and confocal imaging and reminding me to maintain rigour and thoroughness in my work. A special thanks to my labmates - Edward, who inspired me with his true perseverance, especially when it comes to western blots; Max, who made every day infinitely more enjoyable and helped me see the positives of any failed experiment; Minza, for helping me connect the dots of my scientific knowledge and connecting me to many invaluable sources of wisdom; Paul, for his kindness and his patient guidance through the hard times I encountered; Sehrish, for the career advice and for reminding me that life exists outside of work. I would also like to thank my boyfriend for supporting me from a distance as I navigated the ups and downs of this degree.

Finally, a great big thank you to my family – my mother, father, brother, and grandmother and aunt in Korea – to whom I owe everything for their immeasurable moral and emotional support.

Contribution to Original Knowledge

The following thesis summarizes my work during my M.Sc., which contributes to understanding the role of *RAI1*-encompassing 17p11.2 deletions in a human cellular model of Smith-Magenis syndrome. The contributions to original knowledge are outlined below.

Generation of a novel human neuronal model of Smith-Magenis syndrome using patient-derived iPSCs. From the somatic cells of four clinically diagnosed SMS patients with 17p11.2 deletions, we generated human induced pluripotent stem cells (hiPSCs) and differentiated each line (alongside four healthy control iPSC lines) into neural progenitor cells (NPCs) and forebrain neurons. I found that the cellular localization of *RAI1* differs between hiPSCs, hiPSC-derived NPCs, and neurons.

***RAI1*-encompassing 17p11.2 deletions are associated with cellular and neuronal morphological defects.** I found that SMS hiPSC-derived NPCs have reduced proliferation, changes in cell cycle dynamics, increased DNA damage, and increased apoptosis compared to controls. I also found that SMS forebrain neurons have excitatory synaptic defects and morphological defects at the early and late stages of hiPSC-derived neuron maturation.

Contribution of Authors

Literature review and manuscript writing: Yoobin Cho

Supervision: Wei-Hsiang Huang

Revision of project and proposal: Thomas Durcan, Carl Ernst

Experimental ideas: Wei-Hsiang Huang, Yoobin Cho

Cell culture: Yoobin Cho, Yu-Ju Lee, Ya-Ting Chang

hiPSC and NPC immunocytochemistry: Yoobin Cho

Neuron immunocytochemistry: Yoobin Cho, Yu-Ju Lee

Confocal imaging: Yoobin Cho, Max Kowalczyk, Yu-Ju Lee

Immunocytochemistry image processing: Yoobin Cho

Quantitative PCR and cell cycle analysis: Yu-Ju Lee

3D neuron reconstruction: Yoobin Cho

Data analysis and interpretation: Yoobin Cho

List of Tables and Figures

Table 1. Details of hiPSC lines used in the study.

Table 2. Clinical features of SMS patients.

Table 3. Antibodies used for immunofluorescent staining.

Table 4. Imaging parameters used to acquire quantification and representative images.

Figure 1. Single-nucleus RNA sequencing of RAI1 expression in the human prefrontal cortex.

Figure 2. SMS hiPSC deletion sizes and chromosomal abnormalities.

Figure 3. Characterization of hiPSCs.

Figure 4. Characterization of hiPSC-derived NPCs.

Figure 5. NeuN expression in hiPSC-derived forebrain neurons at 6 WPD.

Figure 6. RAI1 expression in hiPSCs, NPCs, and neurons.

Figure 7. Altered cell cycle dynamics in SMS hiPSC-derived NPCs.

Figure 8. Increased DNA damage in SMS hiPSC-derived NPCs and hiPSCs.

Figure 9. Increased apoptosis in SMS hiPSC-derived NPCs.

Figure 10. Altered spine morphology in SMS hiPSC-derived neurons.

Figure 11. Increased excitatory synapse formation in SMS hiPSC-derived neurons.

Figure 12. Soma morphological defects in SMS hiPSC-derived neurons.

Figure 13. Sholl analyses of hiPSC-derived neurons at 4 WPD.

Figure 14. Sholl analyses of hiPSC-derived neurons at 8 WPD.

List of Abbreviations

ASD	Autism spectrum disorder
CNV	Copy number variation
DAPI	4',6-diamidino-2-phenylindole
DDR	DNA damage response
DSB	Double strand break
DSM-5	Diagnostic and Statistical Manual of Mental Disorders, Fifth Edition
E/I	Excitatory/Inhibitory
GABA	Gamma-aminobutyric acid
GAD67	Glutamic acid decarboxylase 67
GAPDH	Glyceraldehyde 3-phosphate dehydrogenase
GFP	Green fluorescent protein
hiPSC	Human induced pluripotent stem cell
KI67	Kiel 67
NANOG	Nanog Homeobox
NDD	Neurodevelopmental disorder
NDS	Normal Donkey Serum
NESTIN	Neuroepithelial stem cell protein
NeuN	Neuronal nuclear protein
NPC	Neural progenitor cell
OCT4	Octamer-binding transcription factor 4
PAX6	Paired Box 6
PBS	Phosphate-buffered saline
pHH3	Phosphohistone-H3
PTLS	Potocki-Lupski syndrome
PSD95	Postsynaptic density protein 95
RAI1	Retinoic acid-induced 1

RT-qPCR	Reverse transcription-quantitative polymerase chain reaction
SMAD	Suppressor of Mothers against Decapentaplegic
SMS	Smith Magenis syndrome
SOX2	SRY (sex determining region Y)-box 2
SSEA-4	Stage-specific embryonic antigen-4
TRA-1-60	T cell receptor alpha locus
VGLUT1	Vesicular glutamate transporter 1
WPD	Weeks post differentiation
CC3	Cleaved caspase-3
mRNA	Messenger ribonucleic acid
myr-GFP	Myristoylated GFP
p53BP1	Phospho-P53 binding protein
γH2AX	γ -H2A histone family member X

1. Introduction

1.1 Human neurodevelopment and neurodevelopmental disorders

The brain is the most complex organ known to humankind, and understanding its development requires integrating knowledge at the systemic, cellular, and molecular levels. Proper formation of the brain requires a precise coordination of cellular processes during early development such as cell proliferation, migration, and maturation, and its accompanying molecular mechanisms. Most of the human population succeeds in generating a highly functional brain that is capable of sensory perception, complex motor outputs, and conducting higher-order cognitive tasks such as social interaction and memory formation; however, some individuals undergo impairments in one or many developmental processes that results in brain deficits collectively called neurodevelopmental disorders (NDDs). The DSM-5 criteria enable the diagnoses of specific NDDs based on distinct symptoms, which differ between patients depending on their genetics and environment. The pathogenesis of these symptoms may converge on some key neurodevelopmental processes including synaptic plasticity, cellular processes during development, and epigenetic regulation.^{1,2}

Autism Spectrum Disorder (ASD) is the most commonly occurring group of NDDs characterized by a spectrum of features that often overlap between cases, including the core features of social interaction deficits, communication impairment, and repetitive behaviours. The current prevalence of ASD is estimated to be 1 in 36 children, affecting approximately 4% of boys and 1% of girls in the United States.³ Twin studies have shown that non-syndromic ASDs are 64%-91% heritable, and genome-wide association studies have identified over 100 converging ASD risk genes (e.g. *RAI1*, *CHD8*, *SCN2A*, *SHANK3*).^{4,5} ASDs are categorized as non-syndromic or syndromic based

on clinical criteria: 75% of cases are non-syndromic, in which only the core ASD phenotypes are present, while syndromic ASDs (~25%) occur with additional clinically distinct features.¹⁰ Post-mortem studies on ASD brains show that the structural development and circuit formation of regions in the cortex, hippocampus, cerebellum, and amygdala are the most affected in ASD.⁷⁻⁹ The main affected cell types include neural stem cells (NSCs) destined for the cortex¹⁰ and cortical excitatory neurons.¹¹ At the signalling level, abnormalities in synaptic transmission caused by neuroinflammation and mitochondrial dysfunction, and altered GABAergic and glutamatergic signaling in the brain is thought to be a main pathogenic mechanism.^{12,13} Despite the expansion of ASD research in the past few decades, our knowledge on the neurobiology of ASD is limited due to the complex interplay between each patient's genetics and their developmental environment.¹² Studies on syndromic ASDs, which tend to have an identifiable genetic cause,⁶ have thus been crucial for understanding the developmental and neurological effects of mutations in specific ASD risk genes.

35% of developmental disabilities and 1% of ASDs are caused by copy number variations (CNVs) and chromosomal abnormalities.¹⁴ CNVs are structural variants in the chromosome such as duplications and deletions of varying genomic sizes. They impact 13% of the human genome, often affecting genes that function in neurodevelopment and can be inherited or occur *de novo*.¹⁵ There are over 50 ASD-related CNVs, which likely affect shared biological pathways such as neuronal development, synaptic function, and chromatin remodeling.¹⁶ The heterogeneity and genetic complexity of CNVs make it difficult to develop a targeted gene therapy for CNV disorders, but they are promising investigation points to uncover the mechanisms disrupted in ASDs. CNVs can be a source of single-gene or monogenic ASDs by altering the expression of a single, dosage-

sensitive gene.⁶ Monogenic disorders are individually rare but together they make up ~5% of all ASDs.⁶ Previous work on monogenic ASDs such as Fragile X syndrome,¹⁷ tuberous sclerosis complex,¹⁸ and RETT syndrome¹⁹ have furthered our understanding of the role of specific ASD risk genes in neurodevelopment. They show a promising convergence of pathological mechanisms that may be common to many ASDs, such as the dysfunction of dendritic morphogenesis, synapse formation, and cell growth during neurodevelopment.⁶ This highlights the wide applicability of research on these rare disorders.

1.2 Human iPSC-derived models of ASD

Developing models that closely recapitulate the complex pathology of non-syndromic ASDs is an important scientific pursuit to better understand ASD etiology and to develop effective treatments. The lack of unifying biomarkers among the spectrum of disorders, along with their genetic and symptomatologic heterogeneity, make it difficult to investigate the biological processes affected in human patients.²⁰ The mouse and the human genome are over 80% homologous, making the mouse an excellent model organism for studying the behavioural and biological effects of ASD-related gene mutations²¹; however, animal models still cannot fully simulate the complex human disease phenotypes of ASDs and do not necessarily represent the etiological mechanisms in humans. *In vitro* human models such as primary cells and human embryonic stem cells can be used to help alleviate these limitations, but each present their own drawbacks including the technical difficulties of acquiring brain tissue for primary cultures and the ethical concerns of using human embryos for research.²² Cell reprogramming has enabled the induction of human somatic cells into human induced pluripotent stem cells (hiPSCs), which bypasses the previously outlined

limitations. This technique involves expressing ectopic transcriptional factors in somatic cells to establish an embryonic stem cell-like state, which are pluripotent and can be propagated indefinitely.²³ hiPSCs can be directly derived from ASD patients' somatic cells to create a practical yet powerful human *in vitro* cellular model that reflects the patients' genetic background. Importantly, patient-derived hiPSCs can be subjected to various differentiation protocols to simulate early human neural development *in vitro* and to generate terminally differentiated cell types.²⁴ In this respect, ASD patient hiPSC-derived neural cells provide access to a previously infeasible model of the cells in the developing human brain.

Most of the neurons that persist throughout an individual's life are generated during telencephalic neurodevelopment; accordingly, the number and activity of pluripotent neural stem cells (NSCs) and multipotent progenitor cells (NPCs) giving rise to these neurons is important. At this stage of neurodevelopment, NSCs and NPCs mediate billions of cycles of cell division,²⁵ differentiation, and apoptosis.²⁶ In addition, they must accurately respond to DNA damage that occurs during replication, transcription, and cellular metabolism. Alterations to such processes can lead to exponentially severe defects in the brain, and insufficient response to DNA damage may result in *de novo* somatic mutations,²⁷ all potentially contributing to the pathogenesis of NDDs.²⁸ Recently, investigating the cellular properties of ASD patient hiPSC-derived NPCs have shown to be a useful tool for identifying the cellular mechanisms affected by specific gene mutations. Indirect methods of neural differentiation, such as dual-SMAD inhibition, consist of using chemicals to inhibit pathways that lead hiPSCs to a non-neuronal fate while activating those that support neuronal differentiation. Compared to the direct (genetic) differentiation methods, this method is more time-consuming and has a lower yield of the desired mature cell type, but it can recapitulate key steps

of natural neurodevelopment *in vitro*. This includes the generation of multipotent NPCs and their differentiation to mature neurons.²⁹ Previously, hiPSC-derived NPCs and forebrain neurons from patients with monogenic disorders such as Rett syndrome¹⁹, Fragile X syndrome¹⁷, and Pherlan-McDermid Syndrome³⁰ have revealed significant NPC dysfunction leading to aberrant neurogenesis and neuronal function.²⁷ Identifying the cellular phenotypes associated with single gene mutations can help elucidate the roles of these genes in important neurodevelopmental processes.

Prenatal cortical neurogenesis in humans involves the generation of a staggering 3.86 million neurons per hour, with 42.3 million synapses forming per minute.³¹ Circuit formation and function are highly sensitive to changes in neuronal differentiation, migration, and synapse formation, and defects in these processes can lead to the well-observed phenotype of excitatory and inhibitory (E/I) imbalances in ASD patients, especially in the cortex.¹¹ The differentiation of ASD patient hiPSC-derived NPCs to forebrain neurons is thus a helpful way to identify the affected processes in corticogenesis.³² Previously, a study of hiPSC-derived pyramidal cortical neurons from ASD patients with *SHANK3* mutations showed that *SHANK3* plays an important role in synaptic formation and function, such as spine density and proportions of spine types.³³ Neuronal morphological phenotypes such as reduced soma size, reduced complexity of dendritic arborization, and altered synaptogenesis with functional changes related to altered E/I balance are also common among ASD patient hiPSC-derived neurons.^{18,26} A paired investigation of hiPSC-derived NPCs and neurons is thus a useful way to delineate the early neurodevelopmental processes and the downstream neuronal changes caused by mutations in ASD risk genes.

1.3 Smith-Magenis syndrome

Smith-Magenis syndrome (SMS) is a rare congenital genetic disorder occurring in approximately 1 of 15000 births.³⁴ It is characterized by developmental delay, epilepsy, obesity, sleep disorders, distinctive physical features such as brachycephaly and broad face, as well as ASD features including speech delay and self-injurious repetitive behaviours.³⁴ SMS affects both sexes equally but ASD prevalence in these patients is greater in females with a 1:3 male-to-female ratio.³⁵ SMS was first reported in 1982 by Ann CM Smith, who observed two patients with an interstitial deletion on chromosome 17p11.2. Over the following decades, Ann Smith and Ellen Magenis diagnosed more unrelated individuals with the same genetic mutation and a similar spectrum of phenotypes.³⁶ Currently, it is estimated that 77% of SMS cases have a 3.7 megabase (Mb) microdeletion in 17p11.2, caused by irregular chromosomal recombination of susceptible repeat elements flanking this region.³⁷ SMS microdeletions encompass approximately 70 protein-coding genes including *Retinoic-Acid Induced 1 (RAI1)*. In the remaining 23% of patients, about 50 pathogenic variants of *RAI1* were detected, largely in-frame and non-sense mutations on exon 3, all leading to *RAI1* haploinsufficiency.³⁴ The core SMS features – especially the neurological and behavioural symptoms – are as severe in patients *RAI1* truncating mutations without 17p11.2 deletions, as those with 17p11.2 microdeletions. The reciprocal disorder of SMS – Potocki-Lupski syndrome (PTLS) – is caused by 17p11.2 and *RAI1* duplication, with phenotypes distinguishable from SMS.³⁸ Together, this suggests that the genes in 17p11.2, especially *RAI1*, are dosage-sensitive genes crucial for neurodevelopment.³⁹

1.4 Retinoic Acid-Induced 1

Though its functions are not fully understood, *RAI1* is an ASD risk gene known to be widely expressed in the body but enriched in the brain, typically localized to the nucleus, and crucial in neurodevelopment.⁴⁰ *RAI1* consists of four protein-coding exons out of six total exons. Among the seven functional domains of *RAI1*, there is a C-terminal “plant homeo-domain” (PHD) with a His-Cys5-His-Cys2-His motif, which is highly conserved across species and involved in chromatin remodeling and transcriptional regulation.⁴¹ The PHD domain of RAI1 is thought to bind to the unmodified histone tail H3,⁴² enabling interactions with PHD-containing proteins. These include PHF14, TCF20, HMG20A, which forms a complex that functions as an epigenetic machinery reader that promotes gene transcription important in neurodevelopment.⁴³ In mouse embryonic stem cells and NPCs, this complex was found to assemble at DNA double-strand breaks (DSBs) to play a role in the DNA damage response (DDR), linking Rai1 to DNA repair and related processes such as cell cycle progression and apoptosis.⁴⁴ In addition, Rai1 mRNA levels are increased during prenatal development and is expressed highly in excitatory and inhibitory neurons, and minimally in glial cells.³⁹ Nascent RNA sequencing of mouse primary cortical neuron cultures also showed that Rai1 is linked to the transcriptional program that responds to reduced network activity, supporting its role as a transcription factor involved in synaptic homeostasis during development.⁴⁵ Further research is required to connect these findings in mouse *Rai1* to human *RAI1*.

1.5 Rodent and cellular models of SMS

As a rare NDD, research on SMS suffers from small sample sizes and relies mostly on clinical studies. Investigating the effects of *Rai1* loss in mouse models have helped identify the potential biological mechanisms underlying the symptoms of this genetic disorder. The first mouse model of SMS was created by deleting the mouse chromosome 11 syntenic to human chromosome 17p11.2, and resulted in SMS-like phenotypes such as hypoactivity, seizures, obesity, craniofacial abnormalities, and motor dysfunction.⁴⁶ Subsequent studies found that mice with a null *Rai1* allele also display SMS-like phenotypes including obesity, craniofacial malformations, increased food intake, and decreased social dominance.^{47,48} Huang and colleagues found that brain-specific heterozygous deletion of *Rai1* (*Nestin^{Cre};Rai1^{flox/+}*) have similar results, supporting that SMS-like neurological phenotypes arise from the central nervous system. The effects of *Rai1* loss in specific regions of the brain have also been studied: in the medial prefrontal cortex, *Rai1* loss results in reduced dendritic spine density of pyramidal neurons⁴⁸; in the hippocampus, *Rai1* loss leads to hyperexcitability without any changes in cell number, axonal projection, or hypertrophy.⁴⁹ Furthermore, a cell-type screen showed that *Rai1* loss from cortical and subcortical excitatory neurons leads to similar phenotypes observed in mice with brain-specific homozygous deletion of *Rai1* (*Nestin^{Cre};Rai1^{CKO}*) such as impaired motor function and associative learning, and increased seizure susceptibility.^{39,49} The gain of 17p11.2 or *Rai1* in these models largely recapitulates opposite phenotypes, associated with PTLN-like features.^{39,46} Overall, the findings point to the *Rai1* dosage sensitivity of cortical excitatory neurons as an important contributor to SMS-like phenotypes in mice. Single-nucleus RNA sequencing in human brains has also shown that RAI1 is enriched specifically in cortical excitatory neurons compared to other cell types and brain regions (Figure 1A).

The cellular and molecular mechanisms of SMS in humans, especially in the brain, are understudied due to the difficulties of acquiring samples. Turco and colleagues derived primary human fibroblasts from patients with 17p11.2 deletions or *RAI1* point mutations and found altered expression of genes related to lipid metabolism, autophagy, and mitochondrial dysfunction.⁵⁰ These findings are aligned with the metabolic phenotypes seen in SMS mouse models, but human neuronal models are required to investigate the mechanisms of neurological phenotypes in SMS. Recently, Altieri and colleagues described the first hiPSC-line derived from an SMS patient,⁵¹ but there are currently no reports on neural cells generated from this model. Generating and characterizing a SMS patient hiPSC-derived NPC and neuronal model is a promising method to identify the pathological mechanisms underlying SMS in humans.

1.6 Rationale and Objectives

SMS is a rare but severe disorder that lacks therapy, and much is left to discover about the effects of *RAII*-encompassing 17p11.2 deletions on human neurodevelopment. The current rodent *Rai1*-loss models of SMS are useful for building an initial understanding of the pathological mechanisms of this condition; still, findings from animal models are not necessarily translatable to human patients. Studying SMS patient brain samples poses technical difficulties and clinical data is insufficient for identifying the cellular mechanisms involved in its pathology. My thesis addresses the need for a human cellular model that faithfully recapitulates the cells in SMS patient brains during neurodevelopment. By investigating SMS patient hiPSC-derived cells, the project investigates the effects of the loss of a several different genes on 17p11.2 which may contribute to the complex clinical manifestations seen in the patients. By generating forebrain NPCs and neurons, the project contributes to uncovering the role of 17p11.2 genes in cortical neurodevelopment and models a brain region highly affected in SMS.

Objective 1. Generate a novel hiPSC-derived neuronal model of SMS.

Objective 2. Characterize the cellular defects of SMS hiPSC-derived forebrain NPCs.

Objective 3. Characterize the synaptic and morphological defects of SMS hiPSC-derived neurons.

***RAII*-encompassing 17p11.2 deletions in humans result in an array of severe neurodevelopmental defects known as SMS, and *Rai1* loss in mouse models results in SMS-like behavioural and physiological phenotypes. I hypothesized that SMS patient hiPSC-derived forebrain NPCs and neurons will show impairments in cellular function, neuronal growth, and synaptic formation due to heterozygous *RAII*-encompassing 17p11.2 deletions.**

2. Materials and Methods

2.1 Subjects and hiPSC lines

The use of eight hiPSC lines was approved by the research ethics board of the Research Institute of the McGill University Health Centre (IRB). Efforts were made to use female and age-matched hiPSC lines (see Table 1 for details on all hiPSC lines). HiPSCs derived from the fibroblasts or leukocytes of two healthy individuals and one SMS patient were obtained from Coriell Institute (Control-1, Control-2, SMS-2) and two healthy hiPSC lines were obtained from the Montreal Neurological Institute (Control-3, Control-4). Three SMS patient-derived fibroblasts were purchased from Coriell Institute (SMS-1: GM25367, SMS-3: GM25371, and SMS-4: GM24311) then reprogrammed into hiPSCs at the Cell Reprogramming Core Facility of CHU Sainte-Justine with the integration-free Sendai virus (Life Technologies). HiPSC single colonies were manually picked and cultured under feeder-free conditions in mTeSR Plus medium (STEMCELL Technologies) on Matrigel hESC-Qualified Matrix (Life Technologies). The established clones were passaged at least 15 times, and one clone from each line was used.

2.2 Cell culture

HiPSCs were maintained in mTeSR Plus medium with the Primocin antimicrobial agent (100µg/ml, InvivoGen) on Matrigel hESC-Qualified Matrix in a 5% CO₂ humidified incubator at 37°C. In preparation for NPC induction, hiPSC colonies were dissociated with Gentle Cell Dissociation Reagent (STEMCELL Technologies) and plated onto Matrigel-coated dishes in mTeSR Plus medium with ROCK inhibitor Y-27632 (STEMCELL Technologies). To obtain

CNS-type NPCs, starting the following day, the cells were cultured in STEMdiff SMADi Neural Induction medium (STEMCELL Technologies). The induction was continued for 21 days then passaged with Accutase (STEMCELL Technologies) and plated onto A) dishes coated with Matrigel and STEMdiff Neural Progenitor medium (STEMCELL Technologies) for further experimentation on NPCs, or onto B) dishes coated with poly-ornithine (Sigma-Aldrich) and laminin (Invitrogen) in STEMdiff Forebrain Neuron Differentiation medium (STEMCELL Technologies) to generate forebrain neuron cultures. The forebrain neurons were incubated for 7 days then plated onto poly-ornithine and laminin-coated dishes in STEMdiff Forebrain Neuron Maturation medium (STEMCELL Technologies). The neurons were maintained in Maturation medium for up to 56 days in a 5% CO₂ humidified incubator at 37°C.

2.3 Quality control of hiPSCs and derived cells

All hiPSC lines were screened as negative for mycoplasma (MycStrip, InvivoGen) prior to culturing, and Short Tandem Repeat (STR) analyses authenticated each line with their respective somatic line. Pluripotency of all hiPSCs lines were assessed by immunostaining for nuclear and surface pluripotency markers (Figure 1). NPC induction was assessed by immunostaining for forebrain NPC markers between days 14 and 21 of incubation in Neural Induction medium (Figure 2). Differentiation to mature neurons was assessed by immunostaining for a neuronal nuclear protein marker after 42 days in Forebrain Neuron Maturation medium (Figure 3).

2.4 RNA extraction and quantitative PCR

Cellular RNA from each cell line was extracted using TRIzol (Invitrogen) according to the manufacturer's instructions. Total complementary DNA (cDNA) were generated by reverse transcriptase reactions using the SuperScript III First-Strand Synthesis System (Thermo Fisher) as per the manufacturer's instructions. 20ng of cDNA was used per reaction with SsoAdvanced Universal SYBR Green Supermix (Bio-Rad) on a Bio-Rad qPCR system. Glyceraldehyde 3-phosphate dehydrogenase (GAPDH) was used as a housekeeping gene for normalization, and gene expression was analyzed using the $2^{-\Delta\Delta Ct}$ method. The normalized expression levels were compared between cell lines. The primers used were the following:

RAI1_Fwd (5'CCTCAGCATTCCCAGTCCTTC3')

RAI1_Rev (5'CTGTGCAACTCTTATAGGAGTGG3')

GAPDH_Fwd (5'AAGGTGAAGGTCGGAGTCAA3')

GAPDH_Rev (5'AATGAAGGGGTCATTGATGG3')

2.5 Immunocytochemistry

HiPSCs and NPCs were plated on glass coverslips coated with Matrigel, and hiPSC-derived neurons were plated on glass coverslips coated with poly-ornithine and laminin. When the desired density or weeks of incubation was reached, the coverslips were transferred to a non-treated 12-well plate and washed with phosphate-buffered saline (PBS) three times, then fixed with 4% paraformaldehyde (15 min at room temperature). Samples were washed three times in

PBS (15 min each), then permeabilized with 0.1% TX-100 in PBS (10-20 min depending cellular localization of protein being stained). Samples were blocked in 2% normal donkey serum (NDS) 5% bovine albumin serum (BSA) in PBS (1 hour at room temperature). Primary antibodies diluted appropriately in fresh blocking solution were added to the samples then incubated overnight at 4°C, away from light (see Table 2 for a full list of antibodies and dilutions). Samples were washed three times in PBS (15 min each at room temperature). Secondary antibodies at 1:2000 dilutions in blocking solution were added to the samples then incubated for 1 hour at room temperature, away from light. Samples were washed three times in PBS (15 min each), then mounted onto glass slides with DAPI Fluoromount-G (SouthernBiotech). Image acquisition was performed on a confocal microscope (Olympus FV-1000 confocal laser scanning microscope) with 10x, 20x, or 60x objectives. Z-stacks were taken with a step size of 0.3µm-3.0µm (see Table 3 for imaging parameters) with a 1024 x 1024 resolution. Image analyses were performed using the Fiji ImageJ software.

2.6 Data acquisition from immunofluorescence images

HiPSC pluripotency marker validation: Merged images were split and colored according to fluorescent channels (DAPI = grey; 647 = cyan, Cy3 = magenta). The DAPI channels were converted to binary, and the Analyze Particles function was used to count the number of DAPI-stained nuclei. For hiPSC, NPC, and neuron markers, DAPI-stained nuclei with the absence of the marker were counted manually using the multi-point tool.

γH2AX and p53BP1 foci quantification: Merged images were split and colored according to fluorescent channels (DAPI = grey; 647 = cyan, Cy3 = magenta). The DAPI channels were used

to generate masked outlines of the nuclei, and the DNA damage foci within each nucleus' outline were counted manually.

Other characterizations: Merged images were split and colored according to fluorescent channels (DAPI = grey; 647 = cyan, Cy3 = magenta). After a similar pre-processing as done for hiPSC images, DAPI⁺ cells co-localized with cyan, magenta, or both were detected using the Colour Threshold function, converted to binary, then counted using Analyze Particles.

2.7 Neuronal morphometric analyses

Forebrain neurons at two different timepoints (4 WPD and 8 WPD) were sparsely infected (MOI = 0.01) with a lentivirus which delivers GFP to myristoylation sites on cell membranes (myr-GFP).⁵² The GFP signal was enhanced using immunocytochemistry, then the slides were imaged on a confocal microscope with a 1024 x 1024 resolution at 10x magnification. Z-stacks were taken with a step size of 1.0 μ m. The neurons were individually reconstructed in 3D using user-guided automatic tracing on the NeuroLucida 360 software Version 2020.3.3 (MBF Biosciences). The hiPSC-derived neurons with 1) pyramidal or ovoid-shaped somas, 2) at least two branched neurites, and 3) all neurites visible by the GFP signal were considered for reconstruction. Sholl analyses were conducted at 4 WPD and 8 WPD. For both timepoints, 10 μ m increments were used to define the gradually increasing radius of concentric circles centering at the centroid of the soma. Global and subtle branching patterns and other morphometric parameters including soma volume, soma surface area, and the summed length of all neurites per neuron, were analyzed using NeuroLucida Explorer (MBF Biosciences).

2.8 Dendritic spine morphometric analyses

For analysis of dendritic spines, hiPSC-derived neurons at 8WPD were transduced with the GFP lentiviral vector and subjected to immunostaining as detailed in 2.7. The slides were imaged on a confocal microscope with a 1024 x 1024 resolution at 60x magnification. Z-stacks were taken with step size of 0.75 μ m. The neurites were traced using user-guided automatic tracing on the NeuroLucida 360 software. Fully visible neurite segments with no overlapping signal were traced for a total of between 300-500 μ m for each hiPSC line.

The spines were automatically detected by the following parameters:

Outer range – 2.5 μ m; Minimum height - 0.3 μ m, Detector sensitivity – 135%; Minimum count – 10 voxels.

The spines were then auto classified by following parameters:

The Head-to-neck ratio - 1.1; Length-to-head ratio - 2.5; Mushroom head size: 0.35 μ m;
Filopodium length: 3 μ m.

The total and classified spine densities and individual spine morphology were analyzed using NeuroLucida Explorer (MBF Biosciences).

2.9 Statistical analyses

The data were analyzed for statistical significance using the GraphPad Prism 0.9 software. Error bars in plots represent the Standard Error of the Mean (SEM). The sample size and statistical tests used for each analysis are indicated in the text and figure legends. For parametric datasets within two groups, a two-tailed Student's t-test with Welch's correction used. For non-

parametric datasets with two groups, an unpaired Mann-Whitney test was performed. For data with more than two groups, analysis of variance (ANOVA) was used. The differences were considered statistically significant as follows:

* $p < 0.05$, ** $p < 0.01$, *** $p < 0.001$, **** $p < 0.0001$.

3. Results

Generation of hiPSC-derived forebrain NPCs and neurons from SMS patients

The induction of SMS patient-derived somatic cells to hiPSCs has been reported only once previously,⁵¹ and there are currently no studies using SMS patient hiPSC-derived neural cells. To generate this novel hiPSC-derived neuronal model of SMS, we first reprogrammed the somatic cells of SMS patients with *RAII*-encompassing 17p11.2 deletions to hiPSC colonies. We derived four SMS hiPSC lines from the fibroblasts of individuals clinically diagnosed with SMS (Table 1, Table 2) with 17p11.2 heterozygous deletions (Figure 2A), and four control hiPSC lines from the fibroblasts or leukocytes of healthy individuals. G-band karyotyping showed that both control and SMS hiPSCs have normal chromosomal patterns excluding the deleted 17p11.2 region in SMS lines (Figure 2B). Spontaneous differentiation to undesired cell types and the immediate health condition of the hiPSC cultures can negatively impact downstream differentiation processes into target cell types; immunostaining confirmed that all hiPSC lines highly expressed endogenous embryonic stem cell markers NANOG, SSEA4, OCT4, and TRA-1-60, with no significant differences between controls and SMS (Figure 3). RT-qPCR showed in SMS hiPSCs, the *RAII* mRNA levels are 30.4% of control *RAII* mRNA levels (Figure 6A), confirming heterozygosity in SMS lines.

We used a dual SMAD-inhibition induction protocol to induce all hiPSCs to NPCs (Figure 4A). Here, we defined NPCs as intermediate forebrain neural progenitors that express the neural stem cell markers PAX6, NESTIN, and SOX2. Immunostaining confirmed that all cultures after 14

days of induction highly expressed these markers with no significant differences between SMS and controls (Figure 4B-F), showing that SMS hiPSCs can be successfully induced to forebrain NPCs. After growing in neural induction media for 7 more days, we passaged the cultures into NPC maintenance media for downstream NPC experiments or into forebrain neuron differentiation media for differentiation to cortical forebrain neurons. RT-qPCR of NPCs in maintenance media confirmed that in SMS NPCs, *RAII* mRNA levels are 32.4% of control *RAII* mRNA levels (Figure 6B), showing that the heterozygosity is maintained after hiPSCs undergo NPC induction. We refer to the hiPSC-derived neuron cultures by the number of weeks post differentiation (WPD), with 0 WPD being the first day of incubation in forebrain neuron differentiation media. The hiPSC-derived neurons were maintained in maturation media for up to 8 WPD with experiments at various points in the maturation timeframe (Figure 3A). Immunostaining for the neuronal nuclear marker NeuN showed a high purity of neurons in the hiPSC-derived neuron cultures at 6 WPD (Figure 5), showing that SMS hiPSCs-derived NPCs can successfully be differentiated to neurons.

RAII is expressed in hiPSCs and throughout their differentiation to NPCs and neurons

RAII has been found to localize to and act as a transcription factor in the nucleus,⁵³ and single cell RNA sequencing has found that RAI1 expression is enriched in cortical excitatory neurons in the human brain (Figure 1A). However, the cellular expression pattern of *RAII* throughout early human neurodevelopment is unknown. To investigate this, I performed immunostaining and quantified the expression of *RAII* in control hiPSCs and throughout their induction and differentiation to NPCs and forebrain neurons, respectively (Figure 6C). In control hiPSCs, *RAII*

is highly expressed (>99%) specifically in the cytosol (Figure 6D). Similarly, *RAII* is highly expressed in control hiPSC-derived NPCs following NPC induction (>99%) but the expression at this point is nuclear (Figure 6E). In the NeuN⁺ cells of hiPSC-derived neurons cultures at 6 WPD, *RAII* is also highly expressed (>98%) and is localized to the nucleus (Figure 6G). The findings suggest that the nuclear localization of *RAII* is related to the differentiated state of hiPSCs, its nuclear localization occurring after induction to forebrain progenitor cells.

Cell cycle dynamics are altered in SMS hiPSC-derived NPCs

hiPSC-derived NPC models TSC, RTT, and macrocephalic ASDs have demonstrated that the mutation of ASD-risk genes contribute to changes in NPC proliferation and cell cycle dynamics via diverse mechanisms, including increased replication stress and increased DSBs.^{6,10,25} We sought to assess whether *RAII*-encompassing 17p11.2 deletions also cause altered cell cycle dynamics in SMS patient hiPSC-derived NPCs. We first performed immunostaining for the proliferation marker antigen KI67, which marks all phases of the cell cycle excluding the G0 phase,⁵⁴ and found that there is a significantly lower percentage of proliferating cells in SMS NPCs (88%) compared to controls (>95%) (Figure 7A-B, 11.31 ± 1.503 % decrease in SMS compared to controls). We observed no significant differences in the mitosis (M) phase marker phospho-Histone H3 (pHH3) (Figure 7C-D), suggesting no difference in the proportion of dividing cells. NPCs with changes in proliferation are likely to have changes in the proportion of cells in each phase of the cell cycle; a reduction in KI67 but no change in pHH3 expression suggests that SMS NPCs are exiting the cycle prematurely and may result in a higher proportion of cells in the G0/G1 phase. The DNA content of cells can be used to determine the proportion of cells in each phase of

the cell cycle, as cells in the G0/G1 growth phase contain half the amount of DNA that those in the G2/M phase have, and cells in the synthesis (S) phase contain intermediate levels. We used propidium iodide for DNA staining and flow cytometry to analyze the cell cycle of SMS and control NPCs. Three biological replicates with 17600-20000 cells per sample were analyzed for each line. We found a consistently greater percentage of cells in the G0/G1 phase and a lower percentage of cells in the S and G2/M phases in SMS NPC samples compared to controls (Figure 7A, 55.26 ± 1.256 % cells in G0/G1 phase increase in SMS compared to controls; 26.63 ± 0.6135 % cells in S phase decrease in SMS compared to controls, 15.21 ± 0.6496 % cells in G2/M phase decrease in SMS compared to controls). This suggests that *RAI1*-encompassing 17p11.2 deletions reduces the proliferation of NPCs by increasing the time spent in the G0/G1 phase.

SMS hiPSCs and NPCs have increased DNA damage

It has previously been found that RAI1 interacts with the PHF14 complex for DNA damage repair at exogenous DNA damage sites.⁴⁴ I tested for DNA damage in hiPSC-derived NPCs by immunostaining for γ H2AX and phospho-53BP1 (p53BP1), which are two independent markers of DNA damage that localize to DNA DSB sites to initiate repair. I observed a significantly higher count of γ H2AX and p53BP1 foci per cell in SMS NPCs compared to controls (Figure 8A-D, 4.115 ± 0.4539 γ H2AX foci per cell increase in SMS compared to controls; 2.210 ± 0.2775 p53BP1 foci per cell increase in SMS compared to controls), suggesting that there is increased DNA damage or increased recruitment of DSB repair proteins in NPCs with *RAI1*-encompassing 17p11.2 deletion. To determine if this phenotype is exclusive to the NPC stage of corticogenesis, I quantified the number of γ H2AX foci per cell in hiPSCs and similarly found a greater average

γ H2AX foci count in SMS hiPSCs compared to controls (Figure 8E-F, 2.380 ± 0.2803 γ H2AX foci per cell increase in SMS compared to controls). Together, this suggests that 17p11.2 deletions affect DNA damage repair dynamics as early as in the embryo.

SMS hiPSC-derived NPCs have increased apoptosis

Irreparable DNA damage may lead to downstream cellular responses that induce cell death, most often by apoptosis.⁵⁵ I assessed this phenomenon in SMS NPC cultures by immunostaining for cleaved caspase-3 (CC3), which is the active form of the apoptosis regulator, caspase 3.⁵⁶ SMS patient hiPSC-derived NPCs have a 6.2% increase in the percentage of cells undergoing apoptosis compared to controls (Figure 9, 6.210 ± 1.052 % increase in SMS compared to controls), suggesting that the altered cell cycle dynamics in SMS may lead to increased programmed cell death.

Spinogenesis is altered in SMS hiPSC-derived forebrain neurons

Sequencing studies have highlighted the role of *Rail* in synaptic formation and signaling (source) and spine density is increased in excitatory pyramidal neurons of *Rail* knockout mice. I investigated whether spinogenesis is altered in SMS hiPSC-derived forebrain neurons. I chose to analyze the spine morphology of SMS hiPSC-derived neurons at 8 WPD, a timepoint at which mature dendritic spines and morphometry is typically observed in hiPSC-derived forebrain neuron cultures.⁵⁷ After transducing the cells with a lentivirus to deliver GFP to myristoylated proteins (myr-GFP) on the cellular membranes, I imaged and reconstructed the dendrites in 3D (Figure

10A) as detailed in the Materials and Methods section. Morphometric analyses showed no significant differences in total spine density nor changes in spine classification proportions between SMS and control neurons (Figure 10B-C). However, quantification of the densities of spine types (thin, stubby, mushroom, filopodia) showed that there is a significant decrease in stubby spine density specifically, in SMS neurons compared to controls (Figure 10D, 0.07786 ± 0.02884 spines/ μm increase in SMS compared to controls). Next, I analyzed the morphology of individual spines and found that SMS hiPSC-derived neurons have significantly greater mean spine volume and mean spine surface areas compared to controls (Figure 10E-F, Volume - $0.4233 \pm 0.2048 \mu\text{m}^3$ increase in SMS compared to controls, Surface Area - $1.257 \pm 0.5615 \mu\text{m}^2$ increase in SMS compared to controls) but no significant changes in mean spine length (Figure 10G). I also found no significant changes in spine head diameter, spine neck diameter, nor the anchor radius (Figure 10H-J). Our analyses show that SMS hiPSC-derived neurons at 6 WPD have an overall spine size compared to controls that is not specifically attributed to spine length, head diameter, or neck diameter.

Excitatory synapse formation is increased in SMS hiPSC-derived forebrain neurons

To investigate the E/I synaptic properties of SMS hiPSC-derived forebrain neurons, we quantified the number of excitatory or inhibitory synapses formed per μm . We defined formed synapses as puncta with colocalized expression of excitatory or inhibitory pre- and post-synaptic markers. For excitatory functional synapses, we quantified the number of puncta/ μm with colocalized expression of vesicular glutamate transporter 1 (VGLUT1) as an excitatory pre-synaptic marker and post-synaptic density (PSD95) as an excitatory post-synaptic marker. We found a significantly

greater number of excitatory puncta formed/ μm in SMS hiPSC-derived neurons compared to controls, with an average of 0.59 excitatory puncta formed/ μm in SMS and an average of 0.26 puncta/ μm in controls (Figure 11A-B, 0.4008 ± 0.0941 puncta/ μm in SMS compared to controls). For inhibitory synapses, we used glutamate decarboxylase (GAD67) as a pre-synaptic inhibitory marker and gephyrin as a post-synaptic marker. Here, we found no significant differences in inhibitory puncta/ μm in SMS compared to controls (Figure 11C-D). Together, these data suggest that 17p11.2 deletions may alter E/I synapse formation during neural circuit assembly, by enhancing the formation of functional excitatory synapses.

Altered neuron morphology in SMS hiPSC-derived forebrain neurons

Previous hiPSC-derived neuronal models of ASD-related CNV disorders show changes in various neuronal morphometric parameters including soma size, neurite length, and neurite complexity.⁵⁸ To investigate these characteristics in SMS hiPSC-derived neurons, we transduced the cultures with myr-GFP then 3D reconstructed individual neurons, as detailed in the Materials and Methods section. We conducted all morphological analyses at 4 WPD and at 8 WPD to identify transient changes during neuronal maturation and differences after maturation, respectively. We analyzed the morphology of somas at both timepoints and found that compared to controls, SMS hiPSC-derived neurons have a significantly greater mean soma volume at 4 WPD (Figure 12A-B, $103.5 \pm 30.34 \mu\text{m}^3$ in SMS compared to controls) but not at 8 WPD (Figure D-E). There were no significant differences in mean soma surface area at either timepoint (Figure C, F). This suggests that neuronal hypertrophy may be a transient characteristic of SMS hiPSC-derived neurons.

This prompted us to investigate whether neuronal size differences are present in morphological features other than the soma (Figure 13, 14). The mean total dendrite length was correspondingly greater in SMS neurons compared to controls at 4WPD (Figure 13C, 128.2 ± 42.26 mean μm in SMS compared to controls); however, this change was reversed at 8 WPD with a lower mean total dendrite length in SMS neurons (Figure 14C, -340.9 ± 127.5 μm in SMS compared to controls). Next, we conducted Sholl analyses to analyze the arborization of hiPSC-derived neurons at 4 WPD (Figure 13F) and at 8 WPD (Figure 14F). At 4 WPD, we found that SMS hiPSC-derived neurons have greater neurite complexity compared to controls at 10, 20, 30, and 40 μm from the soma center (Figure 13B). We quantified the critical radius (the Sholl radius at which a neuron has the greatest number of intersections) and the maximum number of crossings (the greatest number intersections of a neuron) to further investigate these changes. SMS neurons at 4 WPD have no differences in mean critical radii (Figure 13D) but have a significantly greater mean maximum number of crossings compared to controls (Figure 13E, 1.113 ± 0.2675 more crossings in SMS compared to controls). Sholl analyses at 8 WPD showed no significant differences in overall dendrite complexity, in the critical radius, nor in the maximum number of crossings (Figure 14D-E). The results show that SMS neurons are larger and have increased arborization at 4 WPD but have a lower mean total dendrite length and no difference in arborization at 8 WPD.

Discussion

My thesis is the first to use SMS patient hiPSC-derived neural cells to investigate the effects of heterozygous *RAI1*-encompassing 17p11.2 deletions on the early aspects of forebrain neurodevelopment. Increased DNA damage was observed in SMS patient-derived hiPSCs, which persisted after their induction to hiPSC-derived forebrain NPCs. The SMS NPCs showed increased apoptosis, decreased proliferation, and changes in cell cycle dynamics. At 6 WPD, the SMS hiPSC-derived forebrain neurons had increased dendritic spine volume and surface area compared to controls, paired with an increase in excitatory synapse formation. The SMS neurons also showed greater soma volumes, longer total dendrites, and increased dendritic arborization at 4 WPD but not at 8 WPD, indicating a transient morphological overgrowth or accelerated growth at the early stages of forebrain neuron maturation. These results suggest that the cellular phenotypes of 17p11.2 deletions arise as early as in the embryo and alter the cellular properties of the NPCs during early corticogenesis, and eventually leads to morphological defects in differentiated neurons.

A major goal of the project was to generate and validate a novel hiPSC-derived neuronal model of SMS. Previously, one group reported the successful generation of hiPSCs from the skin fibroblasts of a patient with an *RAI1* truncating mutation,⁵¹ but no further characterization nor differentiation to downstream cell types were performed. There are currently no reports on hiPSC-derived models of 17p11.2 CNVs. An hiPSC-derived neuronal model of SMS provides the advantage of reflecting the specific genetic backgrounds of each patient donor, enabling the study of an *in vitro* neurodevelopmental model of this complex human genetic disorder. Using an indirect

differentiation method, which is often used to generate hiPSC-derived neuronal models of ASDs,⁵⁹ we induced SMS patient-derived hiPSCs to NPCs, and then differentiated them to forebrain neurons. We validated the expression of their respective stage markers in each cell type and confirmed *RAI1* heterozygosity before and after NPC induction. This serves as pioneering work for future studies of SMS hiPSC-derived neurons, to uncover the cellular and molecular mechanisms underlying SMS pathology.

We first investigated the cellular localization of RAI1 at different stages of forebrain neuron differentiation of hiPSCs and found it changes from cytosolic to predominantly nuclear as hiPSCs are induced to forebrain NPCs. Its expression remains predominantly nuclear after differentiation to forebrain neurons. RAI1 is generally known to be a nuclear protein acting as a transcription factor in human cells.^{53,60} Its cytosol-specific expression in hiPSCs suggests that RAI1 is not yet translocated to the nucleus during the early embryonic stages of development; instead, it may play a part in different mechanisms specific to the cytoplasm. Retinoic Acid (RA) is a derivative of vitamin A crucial for neuronal differentiation and migration during corticogenesis.^{61,62} Named after its inducibility to retinoic acid, RAI1 thought to interact with different subclasses of retinoic acid receptors (RARs), which were found to colocalize to different cellular regions and have distinct developmental functions depending on the subclass.^{63,64} In the neurons of post-mortem human hippocampi, RAR α and RAR γ were found to colocalize with RAI1 in the nucleus, while RAR β and RAI1 were found to colocalize in the cytoplasm as well as the nucleus.⁶³ Though the downstream functions of each RAR subclass is not fully known, shift of RAI1 expression from cytosolic to nuclear expression after hiPSC induction to NPCs suggests a differential role of RAI1 at different stages of development, perhaps related to the downstream pathways of the RAR

subclasses. This also indicates that RAI1 begins its activity as a transcription factor⁵³ in the nuclei of cells that have passed the early stages of neural induction.

We next identified several cellular phenotypes in SMS hiPSC-derived NPCs by investigating their proliferation, cell cycle, and DNA damage. SMS NPCs have reduced levels of proliferating cells, an increased proportion of cells in the G1 phase, and a decreased proportion of cells in the S and G2/M phases compared to controls. SMS NPCs also have elevated levels of DNA damage compared to controls, shown by greater γ H2AX and p53BP1 foci counts per cell. The molecular trigger for the increased recruitment of these DDR proteins here is unclear; thus, investigating the activation of other points of the DDR pathway can help determine the specific cause of the observed DNA damage. For example, the activation of the ATR-CHK1 pathway can be investigated for increases in replication stress that leads to DNA damage, as found in hiPSC-derived models of macrocephalic autism⁶⁵ and schizophrenia⁶⁶, as well as in mouse models of Rett syndrome⁶⁷. We also found that SMS NPCs have a significantly greater number of cells undergoing apoptosis compared to controls, indicating an increase in irreparable DNA damage. The precise modulation of genome replication and DNA repair is essential during the massive expansion of cells during early corticogenesis, and DDR proteins must be correctly recruited to operate at the proper DSB sites.⁵⁵ Dysfunction in these mechanisms can exponentially affect the proliferation and cell cycle of the dividing pool of NPCs and their downstream differentiation targets. Thus, the increased DNA damage in SMS NPCs here may be a reason for their decreased proliferation, reduction of cells in the S and G2/M phases, and an eventual exit of the cell cycle into apoptosis. The findings are also reminiscent of prior findings in mouse embryonic stem cells, in which Rai1 was found to rapidly localize to exogenously affected DSB sites along with other

components of the DNA damage-responsive Phf14 complex.⁴⁴ As such, SMS hiPSC-derived NPCs may have aberrant DDR mechanisms due to the loss of RAI1. It is possible that with RAI1 loss, DNA repair is stalled at the initial recruitment of γ H2AX and p53BP1, resulting in increased number of foci; alternatively, the loss of RAI1 may lead to increased DDR protein recruitment to DNA damage foci due to other compensatory mechanisms for cellular impairments. Further work is required to elucidate the mechanisms underlying elevated baseline DNA damage levels in SMS hiPSCs and NPCs.

Dendritic spines harbour the main post-synaptic sites of excitatory input⁶⁸ and spine dysgenesis in neurons is thought to underlie the synaptic defects found in ASD.⁶⁹ We analyzed the 3D spine morphology of SMS hiPSC-derived neurons at 6 WPD and found that they have increased spine volume and surface area compared to controls. 3D spine morphology is directly related to synaptic transmission and synapse formation; larger spine volume is positively correlated with the area of the post synaptic density and tends to contain more excitatory AMPA and NMDA receptors than smaller ones.⁷⁰⁻⁷² There were no significant differences in proportion of spine types nor overall spine density in SMS and controls, but the density of stubby spines was lower in SMS hiPSC-derived neurons. Stubby spines are stable spines that are known to form strong excitatory synapses⁷³; the decrease in density of this spine type may serve as a compensatory mechanism for the increased excitatory signaling caused by larger 3D spine morphology. Synaptic upscaling is a mechanism of plasticity by which changes in neuronal activity is regulated by strengthening or weakening the cell's response to input.⁷⁴ The dysregulation of synaptic scaling is a common pathological mechanism found in NDDs such as RTT,⁷⁵ TSC,⁷⁶ and other ASDs.⁷⁷ It was previously shown that RAI1 loss leads to increased synaptic surface expression of AMPA

receptors after activity suppression by TTX, suggesting that *RAI1* loss promotes synaptic upscaling and strengthening.⁴⁵ Our data suggests that *RAI1* loss in our hiPSC-derived neuron model may be promoting synaptic upscaling, leading to increases in 3D spine morphology and changes in spine type density, which may be linked to changes in excitatory synapse formation.

We investigated the colocalization of pre- and post-synaptic markers VGLUT1 and PSD95 and found that SMS neurons have enhanced excitatory synapse formation. The importance of *Rai1* expression in excitatory neurons was previously highlighted in mice, in which *Rai1* haploinsufficiency in subcortical excitatory neurons led to SMS-like phenotypes including obesity, learning and memory, and motor dysfunction.³⁹ *Rai1* haploinsufficiency in hippocampal dentate granule cells also caused increased glutamatergic synaptic transmission and epileptogenesis.⁴⁹ In the mouse embryonic brain, *Rai1* levels become detectable during neurogenesis at E13.5, and continue to increase until they peak at p7, after which mRNA levels decrease and stabilize. *Rai1* levels peak around the same time as cortical microcircuit formation, synapse maturation, dendritic and axonal morphogenesis, circuit refinement, and wiring. During this phase of corticogenesis, neurons become integrated into the cortical network, and cell survival is activity dependent. Cells that are not integrated into nascent networks undergo programmed cell death. During early post-natal stages, there is also a rapid increase in the number of synapses formed, which is followed by a synapse elimination phase, or synaptic 'pruning', which is crucial for the proper development of functional circuits.⁷⁸ Given that the rise in *Rai1* levels coincides with a critical temporal window during corticogenesis, it is possible that *Rai1* plays a role in regulating these processes, thereby maintaining E/I balance. Therefore, *RAI1* loss leading to alterations in these pre-natal neurodevelopmental processes may contribute to common excitation-related SMS symptoms

including epilepsy, repetitive behaviours, and developmental delay.⁷⁹ Together, our results suggest that *RAI1*-encompassing 17p11.2 deletions contribute to E/I imbalances in the brain by altering the dynamics of synaptic structure and excitatory signaling.

Here, we found a transient increase in soma volume, total dendritic length, and arborization in SMS hiPSC-derived neurons compared to controls at 4 WPD. At 8 WPD, the total dendritic length in SMS neurons were lower than in controls, and the other phenotypes were not significantly different from controls. NPC proliferation and cell growth can impact cortical neurons by altering neuronal morphology such as soma size, arborization, and dendrite length. Similarly, 16p11.2 deletion patients at 3 WPD and 6 WPD showed increases in soma size and dendritic length, coupled with increased synaptic function measured by increased miniature excitatory post-synaptic potential amplitude.⁸⁰ Morphological phenotypes were also described in hiPSC-derived neurons modeling Rett syndrome,¹⁹ *TPRC6* haploinsufficiency,⁸¹ and Fragile X syndrome.⁸² As previously reported, RNA-sequencing of the cortex and striatum of *Rai1* conditional knockout mice has shown that *Rai1* regulates genes involved in axon guidance and neuronal morphogenesis, which strongly suggests that it could be an important determinant for soma growth and dendritic formation.³⁹ Thus, *RAI1* may take part in the morphological defects seen in hiPSC-derived neurons.

Similar phenotypes arise in all four of our SMS hiPSC lines despite the varying sizes of 17p11.2 CNVs. This supports that *RAI1* (as the causal gene of SMS that is deleted in all lines) may be a major contributor to the affected mechanisms. However, other genes in the overlapping deleted regions must also be considered. For example, *TOP3A* encodes a DNA topoisomerase that alters DNA topology during transcription,⁸³ which may play a role in the DNA damage phenotype seen

in 17p11.2 deleted hiPSCs and NPCs. *GID4* encodes a protein involved in cellular homeostasis via protein degradation and turnover, which may be a factor in the altered cell cycle dynamics seen in SMS NPCs. *FLII* encodes a protein important for actin cytoskeleton dynamics and actin cytoskeleton remodeling, which may contribute to the morphological changes observed in SMS hiPSC-derived neurons.

One major limitation of this study is that 2D neuron cultures cannot fully recapitulate the complexity of the structure and circuitry of the human brain. This hiPSC-derived model represents only a few cell types of the forebrain, which is a highly heterogeneous region with multiple neuronal subtypes that are interconnected within its own and other brain regions. Generating a 3D cortical organoid model of SMS and investigating the phenotypes identified here will be useful for further modelling the affected circuitry and systemic mechanisms that lead to the neurological phenotypes seen in human patients. In addition, the morphological changes and the enhanced formation of excitatory synapses observed in this study do not show whether they are also functionally affected in SMS hiPSC-derived forebrain neurons. Experiments investigating the electrophysiological properties and network activity of these neurons are thus required to validate the relevance of the observed phenotypes to SMS pathology. As previously explained, another limitation is that this study does not show which gene or genes are responsible for each observed cellular phenotype. Future work should focus on identifying the specific genes involved in these phenotypes by using single-gene knockout hiPSC models or hiPSCs derived from patients with *RAII* loss without other 17p11.2 gene deletions. Future lines of studies should also investigate the potential therapeutic effects of restoring *RAII* in this SMS patient hiPSC-derived neuronal model. Previously, it was shown in a mouse *RaiI* heterozygous knockout model that CRISPR-activation of *RaiI* alleviates

SMS-like phenotypes, suggesting that *Rai1*-haploinsufficient brains are not permanently damaged and may be responsive to therapeutic interventions.⁸⁴ Thus, similar work in SMS hiPSC-derived NPCs and neurons can not only help distinguish the *RAI1* heterozygosity-specific phenotypes from 17p11.2 CNV phenotypes, but also investigate the therapeutic potential of gene therapy in human SMS neurons.

Conclusion and Summary

Regardless of the 17p11.2 deletion sizes, SMS patient hiPSC-derived NPCs have increased DNA damage, which may be linked to the observed phenotypes of decreased proliferation, changes in cell cycle dynamics, and increased apoptosis. SMS hiPSC-derived forebrain neurons also show increased spine size and increased excitatory synapse formation, indicating enhanced excitatory signaling in this disease model. In the early weeks of forebrain neuron maturation (4 WPD), these cells also show morphometric phenotypes such as increased soma size and dendrite arborization, suggestive of accelerated growth that does not persist after maturation (8 WPD). The findings suggest that genes in 17p11.2, namely *RAI1*, plays a critical role in early neurodevelopmental processes including the cell cycle and DDR of forebrain NPCs, excitatory synapse and spine formation, and forebrain neuron morphology. In summary, my thesis provides evidence of specific cellular, morphological, and synaptic mechanisms that may be implicated in SMS pathogenesis, allowing the identification of druggable targets that can support the development of therapies for this incurable disorder.

References

1. LaSalle, J. M. Epigenomic strategies at the interface of genetic and environmental risk factors for autism. *J. Hum. Genet.* **58**, 396–401 (2013).
2. Morris-Rosendahl, D. J. & Crocq, M.-A. Neurodevelopmental disorders—the history and future of a diagnostic concept. *Dialogues Clin. Neurosci.* **22**, 65–72 (2020).
3. Maenner, M. J. Prevalence and Characteristics of Autism Spectrum Disorder Among Children Aged 8 Years — Autism and Developmental Disabilities Monitoring Network, 11 Sites, United States, 2020. *MMWR Surveill. Summ.* **72**, (2023).
4. Forrest, M. P. & Penzes, P. Autism Genetics: Over 100 Risk Genes and Counting. *Pediatr. Neurol. Briefs* **34**, 13.
5. Ronald, A. *et al.* Genetic heterogeneity between the three components of the autism spectrum: a twin study. *J. Am. Acad. Child Adolesc. Psychiatry* **45**, 691–699 (2006).
6. Sztainberg, Y. & Zoghbi, H. Y. Lessons learned from studying syndromic autism spectrum disorders. *Nat. Neurosci.* **19**, 1408–1417 (2016).
7. Weston, C. S. E. Four Social Brain Regions, Their Dysfunctions, and Sequelae, Extensively Explain Autism Spectrum Disorder Symptomatology. *Brain Sci.* **9**, 130 (2019).
8. McPartland, J. C., Coffman, M. & Pelphrey, K. A. Recent Advances in Understanding the Neural Bases of Autism Spectrum Disorder. *Curr. Opin. Pediatr.* **23**, 628–632 (2011).
9. Wegiel, J. *et al.* Stereological study of the neuronal number and volume of 38 brain subdivisions of subjects diagnosed with autism reveals significant alterations restricted to the striatum, amygdala and cerebellum. *Acta Neuropathol. Commun.* **2**, 141 (2014).
10. Ernst, C. Proliferation and Differentiation Deficits are a Major Convergence Point for Neurodevelopmental Disorders. *Trends Neurosci.* **39**, 290–299 (2016).
11. Hollestein, V. *et al.* Excitatory/inhibitory imbalance in autism: the role of glutamate and GABA gene-sets in symptoms and cortical brain structure. *Transl. Psychiatry* **13**, 1–9 (2023).
12. Gevezova, M. *et al.* Autistic spectrum disorder (ASD) – Gene, molecular and pathway signatures linking systemic inflammation, mitochondrial dysfunction, transsynaptic signalling, and neurodevelopment. *Brain Behav. Immun. - Health* **30**, 100646 (2023).

13. Al Dera, H. Cellular and molecular mechanisms underlying autism spectrum disorders and associated comorbidities: A pathophysiological review. *Biomed. Pharmacother.* **148**, 112688 (2022).
14. Firth, H. V. *et al.* DECIPHER: Database of Chromosomal Imbalance and Phenotype in Humans Using Ensembl Resources. *Am. J. Hum. Genet.* **84**, 524–533 (2009).
15. Javed, S., Selliah, T., Lee, Y.-J. & Huang, W.-H. Dosage-sensitive genes in autism spectrum disorders: From neurobiology to therapy. *Neurosci. Biobehav. Rev.* **118**, 538–567 (2020).
16. Pinto, D. *et al.* Convergence of Genes and Cellular Pathways Dysregulated in Autism Spectrum Disorders. *Am. J. Hum. Genet.* **94**, 677–694 (2014).
17. Telias, M., Segal, M. & Ben-Yosef, D. Neural differentiation of fragile X human embryonic stem cells reveals abnormal patterns of development despite successful neurogenesis. *Dev. Biol.* **374**, 32–45 (2013).
18. Cheffer, A. *et al.* Human stem cell-based models for studying autism spectrum disorder-related neuronal dysfunction. *Mol. Autism* **11**, 99 (2020).
19. Marchetto, M. C. N. *et al.* A model for neural development and treatment of Rett Syndrome using human induced pluripotent stem cells. *Cell* **143**, 527–539 (2010).
20. Kazdoba, T. M. *et al.* Translational Mouse Models of Autism: Advancing Toward Pharmacological Therapeutics. *Curr. Top. Behav. Neurosci.* **28**, 1–52 (2016).
21. Lander, E. S. *et al.* Initial sequencing and analysis of the human genome. *Nature* **409**, 860–921 (2001).
22. Li, Z. & Zhou, Q. Cellular models for disease exploring and drug screening. *Protein Cell* **1**, 355–362 (2010).
23. Takahashi, K. *et al.* Induction of pluripotent stem cells from adult human fibroblasts by defined factors. *Cell* **131**, 861–872 (2007).
24. Dolmetsch, R. & Geschwind, D. H. The human brain in a dish: The promise of iPSC-derived neurons. *Cell* **145**, 831–834 (2011).
25. Wang, M. *et al.* Increased neural progenitor proliferation in a hiPSC model of autism induces replication stress-associated genome instability. *Cell Stem Cell* **26**, 221-233.e6 (2020).
26. Marchetto, M. C. *et al.* Altered proliferation and networks in neural cells derived from idiopathic autistic individuals. *Mol. Psychiatry* **22**, 820–835 (2017).

27. Villa, C., Combi, R., Conconi, D. & Lavitrano, M. Patient-Derived Induced Pluripotent Stem Cells (iPSCs) and Cerebral Organoids for Drug Screening and Development in Autism Spectrum Disorder: Opportunities and Challenges. *Pharmaceutics* **13**, 280 (2021).
28. McConnell, M. J. *et al.* Intersection of diverse neuronal genomes and neuropsychiatric disease: The Brain Somatic Mosaicism Network. *Science* **356**, eaal1641 (2017).
29. Talias, M. Neural differentiation protocols: how to choose the correct approach. *Neural Regen. Res.* **18**, 1273–1274 (2022).
30. Shcheglovitov, A. *et al.* Shank3 and IGF1 Restore Synaptic Deficits in Neurons from 22q13 Deletion Syndrome Patients. *Nature* **503**, 267–271 (2013).
31. Silbereis, J. C., Pochareddy, S., Zhu, Y., Li, M. & Sestan, N. The Cellular and Molecular Landscapes of the Developing Human Central Nervous System. *Neuron* **89**, 248–268 (2016).
32. Vitrac, A. & Cloëz-Tayarani, I. Induced pluripotent stem cells as a tool to study brain circuits in autism-related disorders. *Stem Cell Res. Ther.* **9**, 226 (2018).
33. Gouder, L. *et al.* Altered spinogenesis in iPSC-derived cortical neurons from patients with autism carrying de novo SHANK3 mutations. *Sci. Rep.* **9**, 94 (2019).
34. Rinaldi, B. *et al.* Smith-Magenis Syndrome—Clinical Review, Biological Background and Related Disorders. *Genes* **13**, 335 (2022).
35. Nag, H. E., Nordgren, A., Anderlid, B.-M. & Nærland, T. Reversed gender ratio of autism spectrum disorder in Smith-Magenis syndrome. *Mol. Autism* **9**, 1 (2018).
36. Smith, A. C. *et al.* Interstitial deletion of (17)(p11.2p11.2) in nine patients. *Am. J. Med. Genet.* **24**, 393–414 (1986).
37. Elsea, S. H. & Girirajan, S. Smith–Magenis syndrome. *Eur. J. Hum. Genet.* **16**, 412–421 (2008).
38. Elsea, S. H. & Williams, S. R. Smith–Magenis syndrome: haploinsufficiency of RAI1 results in altered gene regulation in neurological and metabolic pathways. *Expert Rev. Mol. Med.* **13**, e14 (2011).
39. Huang, W.-H. *et al.* Molecular and Neural Functions of Rai1 , the Causal Gene for Smith-Magenis Syndrome. *Neuron* **92**, 392–406 (2016).
40. Falco, M., Amabile, S. & Acquaviva, F. RAI1 gene mutations: mechanisms of Smith–Magenis syndrome. *Appl. Clin. Genet.* **10**, 85–94 (2017).

41. Bi, W. *et al.* Mutations of RAI1, a PHD-containing protein, in nondeletion patients with Smith-Magenis syndrome. *Hum. Genet.* **115**, 515–524 (2004).
42. Epigenetic Etiology of Intellectual Disability - PMC.
<https://www.ncbi.nlm.nih.gov/pmc/articles/PMC5678009/>.
43. Jones, W. D. *et al.* De Novo Mutations in MLL Cause Wiedemann-Steiner Syndrome. *Am. J. Hum. Genet.* **91**, 358–364 (2012).
44. Käsper, E.-L. *et al.* The neurodevelopmental disorder-linked PHF14 complex that forms biomolecular condensates detects DNA damage and promotes repair. 2021.10.12.462922 Preprint at <https://doi.org/10.1101/2021.10.12.462922> (2021).
45. Garay, P. M. *et al.* RAI1 Regulates Activity-Dependent Nascent Transcription and Synaptic Scaling. *Cell Rep.* **32**, 108002 (2020).
46. Walz, K., Paylor, R., Yan, J., Bi, W. & Lupski, J. R. Rail duplication causes physical and behavioral phenotypes in a mouse model of dup(17)(p11.2p11.2). *J. Clin. Invest.* **116**, 3035–3041 (2006).
47. Bi, W. *et al.* Inactivation of Rail in mice recapitulates phenotypes observed in chromosome engineered mouse models for Smith-Magenis syndrome. *Hum. Mol. Genet.* **14**, 983–995 (2005).
48. Huang, W.-H. *et al.* Early adolescent Rail reactivation reverses transcriptional and social interaction deficits in a mouse model of Smith–Magenis syndrome. *Proc. Natl. Acad. Sci.* **115**, 10744–10749 (2018).
49. Chang, Y.-T. *et al.* Loss of Rail enhances hippocampal excitability and epileptogenesis in mouse models of Smith-Magenis syndrome. *Proc. Natl. Acad. Sci. U. S. A.* **119**, e2210122119 (2022).
50. Turco, E. M. *et al.* Retinoic acid-induced 1 gene haploinsufficiency alters lipid metabolism and causes autophagy defects in Smith-Magenis syndrome. *Cell Death Dis.* **13**, 1–16 (2022).
51. Altieri, F. *et al.* Production and characterization of CSSI003 (2961) human induced pluripotent stem cells (iPSCs) carrying a novel puntiform mutation in RAI1 gene, Causative of Smith–Magenis syndrome. *Stem Cell Res.* **28**, 153–156 (2018).
52. Kameda, H. *et al.* Targeting green fluorescent protein to dendritic membrane in central neurons. *Neurosci. Res.* **61**, 79–91 (2008).

53. Carmona-Mora, P. *et al.* Functional and cellular characterization of human Retinoic Acid Induced 1 (RAI1) mutations associated with Smith-Magenis Syndrome. *BMC Mol. Biol.* **11**, 63 (2010).
54. Bruno, S. & Darzynkiewicz, Z. Cell cycle dependent expression and stability of the nuclear protein detected by Ki-67 antibody in HL-60 cells. *Cell Prolif.* **25**, 31–40 (1992).
55. Plesca, D., Mazumder, S. & Almasan, A. DNA Damage Response and Apoptosis. *Methods Enzymol.* **446**, 107–122 (2008).
56. Ramuz, O. *et al.* Constitutive nuclear localization and initial cytoplasmic apoptotic activation of endogenous caspase-3 evidenced by confocal microscopy. *Int. J. Exp. Pathol.* **84**, 75–81 (2003).
57. Gouder, L. *et al.* Altered spinogenesis in iPSC-derived cortical neurons from patients with autism carrying de novo SHANK3 mutations. *Sci. Rep.* **9**, 94 (2019).
58. Connacher, R. *et al.* Autism NPCs from both idiopathic and CNV 16p11.2 deletion patients exhibit dysregulation of proliferation and mitogenic responses. *Stem Cell Rep.* **17**, 1380–1394 (2022).
59. Ross, P. J. *et al.* Modeling neuronal consequences of autism-associated gene regulatory variants with human induced pluripotent stem cells. *Mol. Autism* **11**, 33 (2020).
60. RAI1 - Antibodies - The Human Protein Atlas.
<https://www.proteinatlas.org/ENSG00000108557-RAI1/summary/antibody>.
61. Gudas, L. J. & Wagner, J. A. RETINOIDS REGULATE STEM CELL DIFFERENTIATION. *J. Cell. Physiol.* **226**, 322–330 (2011).
62. Easwaran, V., Pishvaian, M., Salimuddin, null & Byers, S. Cross-regulation of beta-catenin-LEF/TCF and retinoid signaling pathways. *Curr. Biol. CB* **9**, 1415–1418 (1999).
63. Fragoso, Y. D., Shearer, K. D., Sementilli, A., de Carvalho, L. V. & McCaffery, P. J. High expression of retinoic acid receptors and synthetic enzymes in the human hippocampus. *Brain Struct. Funct.* **217**, 473–483 (2012).
64. Fragoso, Y. D. *et al.* Expression in the human brain of retinoic acid induced 1, a protein associated with neurobehavioural disorders. *Brain Struct. Funct.* **220**, 1195–1203 (2015).
65. Wang, M. *et al.* Increased Neural Progenitor Proliferation in a hiPSC Model of Autism Induces Replication Stress-Associated Genome Instability. *Cell Stem Cell* **26**, 221-233.e6 (2020).

66. Yoon, K.-J. *et al.* Modeling a Genetic Risk for Schizophrenia in iPSCs and Mice Reveals Neural Stem Cell Deficits Associated with Adherens Junctions and Polarity. *Cell Stem Cell* **15**, 79–91 (2014).
67. Pizzamiglio, L. *et al.* The DNA repair protein ATM as a target in autism spectrum disorder. *JCI Insight* **6**, e133654.
68. Muller, D. & Nikonenko, I. Chapter 6 - Dendritic Spines. in *Neural Circuit Development and Function in the Brain* (eds. Rubenstein, J. L. R. & Rakic, P.) 95–108 (Academic Press, 2013). doi:10.1016/B978-0-12-397267-5.00145-X.
69. Phillips, M. & Pozzo-Miller, L. Dendritic spine dysgenesis in autism related disorders. *Neurosci. Lett.* **601**, 30–40 (2015).
70. Harris, K. M., Jensen, F. E. & Tsao, B. Three-dimensional structure of dendritic spines and synapses in rat hippocampus (CA1) at postnatal day 15 and adult ages: implications for the maturation of synaptic physiology and long-term potentiation [published erratum appears in *J Neurosci* 1992 Aug;12(8):following table of contents]. *J. Neurosci.* **12**, 2685–2705 (1992).
71. Matsuzaki, M., Honkura, N., Ellis-Davies, G. C. R. & Kasai, H. Structural basis of long-term potentiation in single dendritic spines. *Nature* **429**, 761–766 (2004).
72. Matsuzaki, M. *et al.* Dendritic spine geometry is critical for AMPA receptor expression in hippocampal CA1 pyramidal neurons. *Nat. Neurosci.* **4**, 1086–1092 (2001).
73. Long-term in vivo imaging of experience-dependent synaptic plasticity in adult cortex - PubMed. <https://pubmed.ncbi.nlm.nih.gov/12490942/>.
74. Abbott, L. F. & Nelson, S. B. Synaptic plasticity: taming the beast. *Nat. Neurosci.* **3 Suppl**, 1178–1183 (2000).
75. Soden, M. E. & Chen, L. Fragile X Protein FMRP Is Required for Homeostatic Plasticity and Regulation of Synaptic Strength by Retinoic Acid. *J. Neurosci.* **30**, 16910–16921 (2010).
76. Zhong, X., Li, H. & Chang, Q. MeCP2 Phosphorylation Is Required for Modulating Synaptic Scaling through mGluR5. *J. Neurosci.* **32**, 12841–12847 (2012).
77. Bourgeron, T. From the genetic architecture to synaptic plasticity in autism spectrum disorder. *Nat. Rev. Neurosci.* **16**, 551–563 (2015).
78. Kast, R. J. & Levitt, P. Precision in the development of neocortical architecture: From progenitors to cortical networks. *Prog. Neurobiol.* **175**, 77–95 (2019).

79. Smith, A. C. *et al.* Smith-Magenis Syndrome. in *GeneReviews*® (eds. Adam, M. P. *et al.*) (University of Washington, Seattle, 1993).
80. Cellular Phenotypes in Human iPSC-Derived Neurons from a Genetic Model of Autism Spectrum Disorder. *Cell Rep.* **21**, 2678–2687 (2017).
81. Griesi-Oliveira, K. *et al.* Modeling non-syndromic autism and the impact of TRPC6 disruption in human neurons. *Mol. Psychiatry* **20**, 1350–1365 (2015).
82. Doers, M. E. *et al.* iPSC-Derived Forebrain Neurons from FXS Individuals Show Defects in Initial Neurite Outgrowth. *Stem Cells Dev.* **23**, 1777–1787 (2014).
83. Pommier, Y., Nussenzweig, A., Takeda, S. & Austin, C. Human topoisomerases and their roles in genome stability and organization. *Nat. Rev. Mol. Cell Biol.* **23**, 407–427 (2022).
84. Chang, H.-C. *et al.* rAAV-CRISPRa therapy corrects Rai1 haploinsufficiency and rescues selective disease features in Smith-Magenis syndrome mice. *J. Biol. Chem.* **299**, 102728 (2023).

Tables and Figures

Table 1. Details of hiPSC lines used in the study.

Name	Source	Disease	Genomic deletions	Biopsy Source	Tissue Type	Race	Sex	Age
Control-1	GM23279	Apparently healthy	None	Skin	hiPSC	Caucasian	Female	36 years
Control-2	GM23720	Apparently healthy	None	B-Lymphocyte	hiPSC	Caucasian	Female	22 years
Control-3	AJC001-5	Apparently healthy	None	Skin	hiPSC	Caucasian	Male	37 years
Control-4	GM25975	Apparently healthy	None	Skin	hiPSC	Caucasian	Female	37 years
SMS-1	GM25367	SMS	Chr17 del:15,175,307-21,519,100	Skin	hiPSC	Caucasian	Female	21 years
SMS-2	GM27918	SMS	Chr17 del:16,881,282-20,121,029	Skin	hiPSC	Caucasian	Female	20 years
SMS-3	GM25371	SMS	Chr17 del:16,769,800-20,126,017	Skin	hiPSC	Caucasian	Female	12 years
SMS-4	GM24311	SMS	Chr17 del:15,777,172-20,554,628	Skin	hiPSC	Caucasian	Female	23 years

Table 2. Clinical features of SMS patients.

SMS patients	Clinical features
SMS-1	Diagnosed at age 7 years via FISH test; brachycephaly; midface retrusion (hypoplasia); broad nasal bridge; down-turned upper lip; prognathism; synophrys; defective vision; strabismus; hearing defect; decreased pain sensitivity; dental abnormalities; hoarse voice; pes planus; scoliosis; syndactyly; tetralogy of Fallot; constipation; short stature; overweight/obesity; high total cholesterol; self-injurious behavior
SMS-2	Diagnosed at age 2 years via FISH test; breech pregnancy; laryngomalacia; defective vision; hearing defect; decreased pain sensitivity; coloboma; midface retrusion (hypoplasia); dental abnormalities; down-turned upper lip; scoliosis; cardiac issues include: ASD, VSD, pulmonary stenosis; intellectual disability (52 IQ/DQ); self-injurious behavior
SMS-3	Diagnosed at 9 years of age; brachycephaly; large forehead; down-turned upper lip; hearing defect; hypotonia; decreased pain sensitivity; abnormal gait; brachydactyly; pes planus; scoliosis; constipation; short stature; speech delay; overweight/obese; decreased tolerance to exercise; intellectual disability; sleep disturbance; self-hugging; immunologic abnormalities; ear infections
SMS-4	Diagnosed at 14 years; dysmorphic facial features; hypotelorism; dental abnormalities; hoarse voice; dry skin; brachydactyly; scoliosis; short stature; hypotonia; obesity; defective vision, strabismus; hearing defect; ataxia, decreased pain sensitivity; constipation; fine motor delay; gross motor delay; speech delay; intellectual disability; ADHD; oppositional defiant disorder; obsessive compulsive disorder; sleep disturbance; repetitive behaviors; self-injurious behaviors; anxiety disorder; disruptive behavior disorder; high total cholesterol

Table 3. Antibodies used for immunofluorescent staining.

Antibody	Species	Catalog	Dilution
NANOG	Rabbit	Abcam ab109250	1:250
SSEA4	Mouse	Abcam ab16287	1:100
OCT4	Rabbit	Abcam ab19857	1:100
TRA-1-60	Mouse	Abcam ab16288	1:500
RAI1	Rabbit	In-house	1:250
PAX6	Rabbit	Cedarlane 901302	1:100
NESTIN	Mouse	Millipore MAB5326	1:250
SOX2	Rabbit	Abcam ab97959	1:100
γ H2AX	Mouse	Cell Signaling Technology 80312S	1:400
p53BP1	Rabbit	Cell Signaling Technology 2675S	1:100
pHH3	Mouse	Cell Signaling Technology 9706S	1:400
CC3	Rabbit	Cell Signaling Technology 9661S	1:400
KI67	Mouse	Sigma MAB4190-25UG	1:1000
CAMKII	Mouse	Abcam ab22609	1:500
DLX5	Rabbit	Thermo-Fisher PA5-101134	1:250
NEUN	Rabbit	Abcam ab177487	1:300
PSD95	Mouse	Abcam Ab2723	1:500
VGLUT1	Guinea Pig	Millipore Ab5905	1:2500
MAP2	Chicken	Abcam Ab5392	1:5000
GEPHYRI N	Mouse	Synaptic Systems 147011(SY)	1:200
GAD65	Guinea Pig	Synaptic Systems 198 104	1:1000
GFP	Chicken	Abcam ab13970	1:250

Table 4. Imaging parameters used to acquire quantification and representative images.

Cell Type	ICC Antibody	Image for quantification (Epifluorescent microscope or Confocal)	Representative Image (Confocal)
hiPSC	Oct4 + TRA-1-60	Epifluo 10X OR Confocal 10X, 4us/pix	20X Oil, 10us/pix
	Nanog + SSEA4	Epifluo 10X OR Confocal 10X, 4us/pix	20X Oil, 10us/pix
NPC	RAI1	Epifluo 10X	20X Oil, 10us/pix
	γ H2AX	Confocal 60X Oil, 10us/pix	60X Oil, 12.5us/pix
	Pax6 + Nestin	Epifluo 10X OR Confocal 10X, 4us/pix	40X Oil, 10us/pix
	Sox2	Epifluo 10X	40X Oil, 10us/pix
	RAI1	Epifluo 10X	40X Oil, 10us/pix
	Ki67	Confocal 10X, 4us/pix	20X Oil, 10us/pix
	γ H2AX	Epifluo 10X	60X Oil, 12.5us/pix
	pHH3	Confocal 10X, 4us/pix	20X Oil, 10us/pix
	CC3	Epifluo 10X	20X Oil, 10us/pix
	p53BP1	Confocal 60X Oil, 10us/pix	60X Oil, 12.5us/pix
Neuron	DLX5 + CAMKII	Confocal 10X, 8us/pix	20X, 10us/pix
	MAP2 + VGLUT1 + PSD95	Confocal 60X Oil, 10us/pix	60X Oil, 14us/pix
	MAP2 + GAD65 + GEPHYRIN	Confocal 60X Oil, 10us/pix	60X Oil, 14us/pix
	NeuN	Confocal 20X	20X, 10us/pix
	GFP (Neuron Morph.)	Confocal 10X, 8us/pix	N/A
	GFP (Spine Morph.)	Confocal 60X Oil, 12.5us/pix	N/A

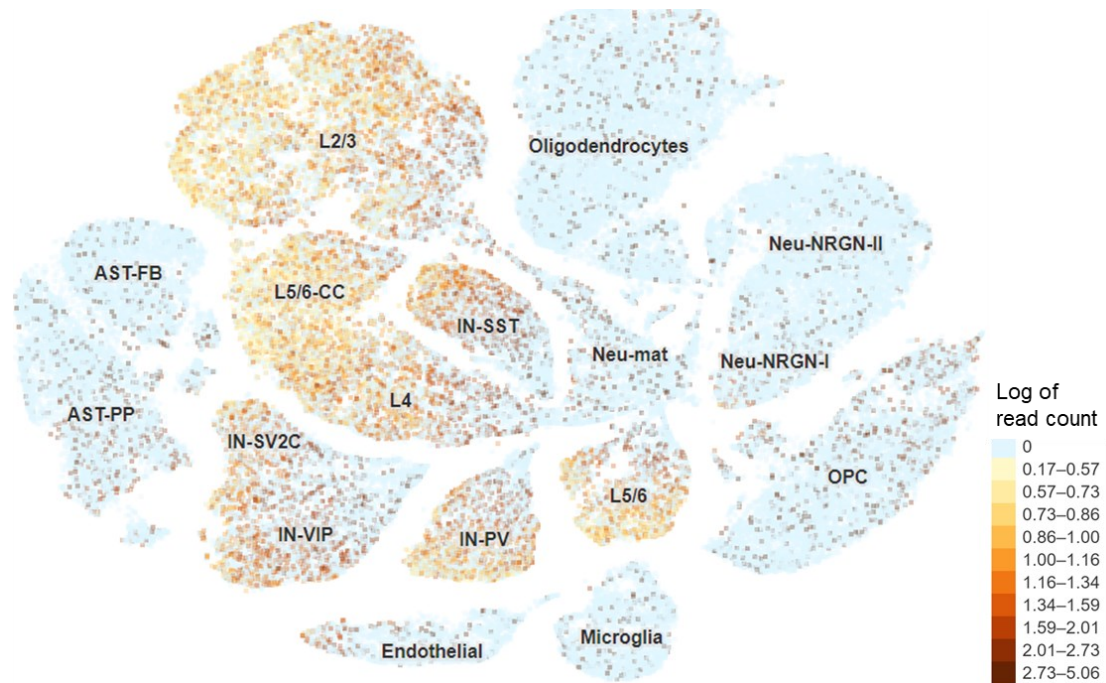


Figure 1. Single-nucleus RNA sequencing of RAI1 expression in the human prefrontal cortex.

Sequencing data from healthy controls and ASD patients sourced from the UCSC cell browser [<https://cells.ucsc.edu>]. RAI1 is enriched in cortical neurons. AST-FB, fibrous astrocytes; AST-PP, protoplasmic astrocytes; OPC, oligodendrocyte precursor cells; IN-PV, parvalbumin interneurons; IN-SST, somatostatin interneurons; IN-SV2C, SV2C interneurons; IN-VIP, VIP interneurons; L2/3, layer 2/3 excitatory neurons; L4, layer 4 excitatory neurons; L5/6, layer 5/6 corticofugal projection neurons; L5/6-CC, layer 5/6 cortico-cortical projection neurons; Neu-mat, maturing neurons; Neu-NRGN-I, NRGN-expressing neurons; Neu-NRGN-II, NRGN-expressing neurons.

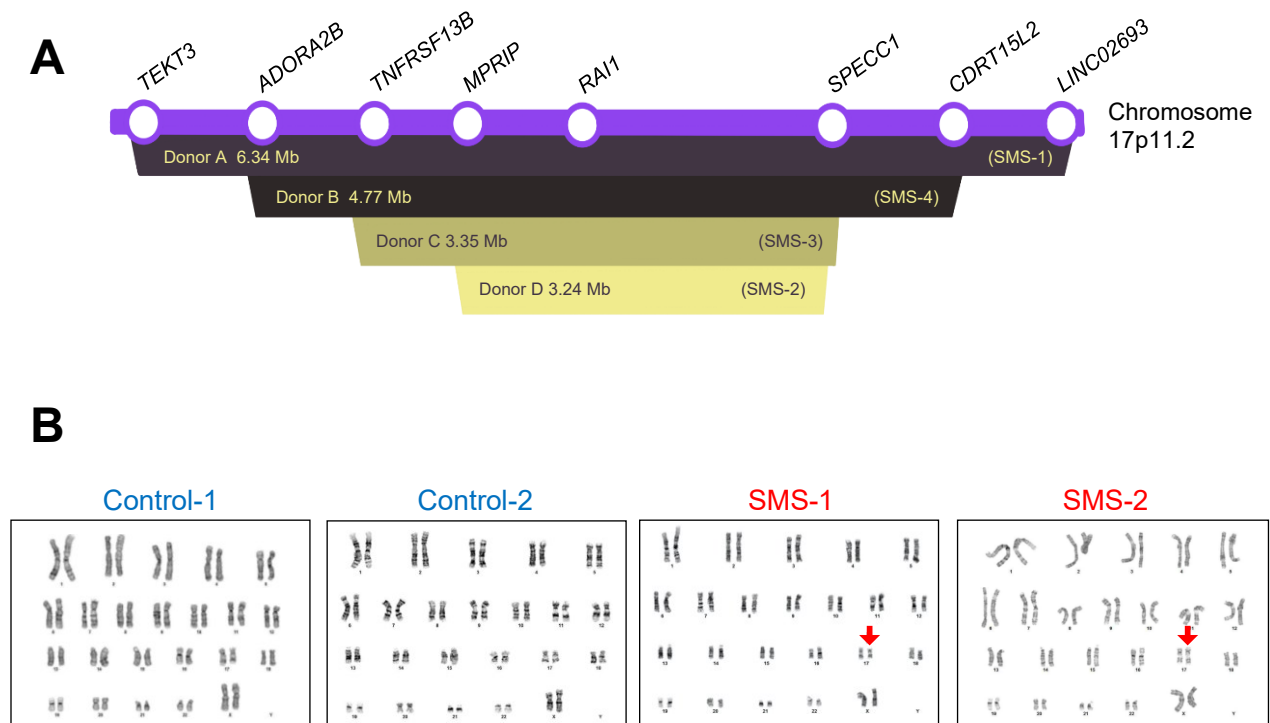


Figure 2. SMS hiPSC deletion sizes and chromosomal abnormalities.

A. Schematic diagram of 17p11.2 deletion sizes in each SMS patient, including the final genes deleted at the extremities of the CNV (not to scale). From left to right: Tektin 3 (*TEKT3*); Adenosine A2b receptor (*ADORA2B*); TNF receptor superfamily member 13B (*TNFRSF13B*); Myosin phosphatase Rho interacting protein (*MPRIP*); Sperm antigen with calponin homology and coiled-coil domains 1 (*SPECC1*); CMT1A duplicated region transcript 15-like 2 (*CDRT15L2*); Chromosome 17 open reading frame 51 (*LINC02693*).

B. Representative karyograms of control and SMS hiPSCs. 17p11.2 CNVs detected in SMS lines, otherwise normal.

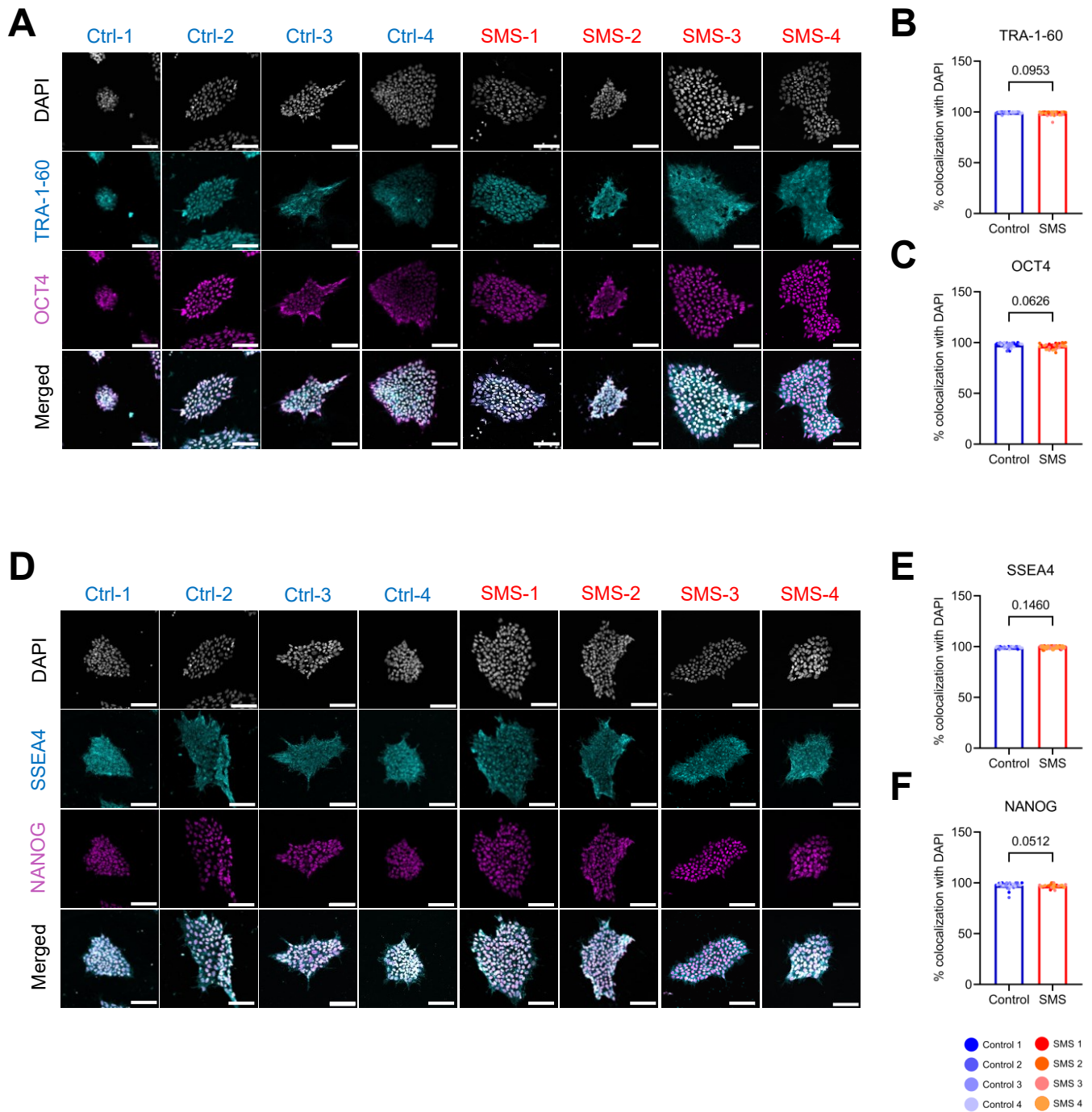


Figure 1. Characterization of hiPSCs.

A. Immunofluorescence staining of control and SMS hiPSC colonies stained with TRA-1-60 (cyan) and OCT4 (magenta). (Scale bar: 100 μ m).

- B. Quantification of control and SMS hiPSCs expressing TRA-1-60 (n = 32 hiPSC colonies per condition, each point represents 1 colony coloured based on genotype.)
- C. Quantification of control and SMS hiPSCs expressing OCT4 (n = 32 hiPSC colonies per condition, each point represents 1 colony coloured based on genotype.)
- D. Control and SMS hiPSC colonies stained with SSEA4 (cyan) and NANOG (magenta). (Scale bar: 100µm).
- E. Quantification of control and SMS hiPSCs expressing SSEA4 (n = 32 hiPSC colonies per condition, each point represents 1 colony coloured based on genotype.)
- F. Quantification of control and SMS hiPSCs expressing NANOG (n = 32 hiPSC colonies per condition, each point represents 1 colony coloured based on genotype.)
- Data presented as means ± S.E.M.; p value by Mann Whitney test.

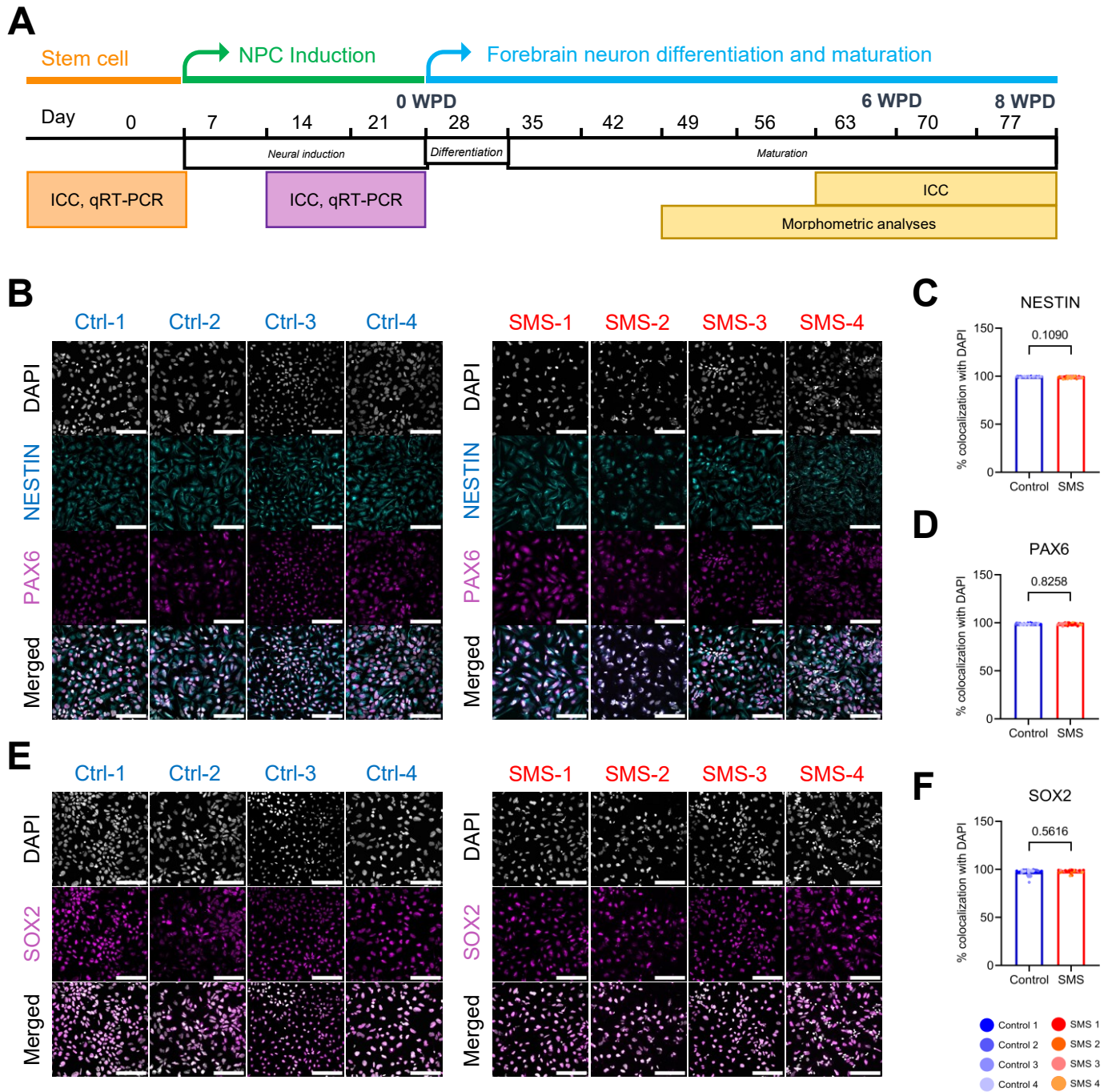


Figure 4. Characterization of hiPSC-derived NPCs.

A. Schematic diagram of neural induction and differentiation from hiPSCs using a monolayer protocol, denoting timepoints of experiments.

B. Immunofluorescence staining of control and SMS hiPSC-derived NPCs stained with NESTIN (cyan) and PAX6 (magenta). (Scale bar: 100 μ m).

C. Quantification of control and SMS hiPSC-derived NPCs expressing NESTIN (n = 32 images per condition, each point represents 1 image coloured based on genotype.)

D. Quantification of control and SMS hiPSC-derived NPCs expressing PAX6 (n = 32 images per condition, each point represents 1 image coloured based on genotype.)

E. hiPSC-derived NPCs stained with SOX2 (magenta). (Scale bar: 100 μ m).

F. Quantification of control and SMS hiPSC-derived NPCs expressing SOX2 (n = 32 images per condition, each point represents 1 image coloured based on genotype.)

Data presented as means \pm S.E.M.; p value by Mann Whitney test.

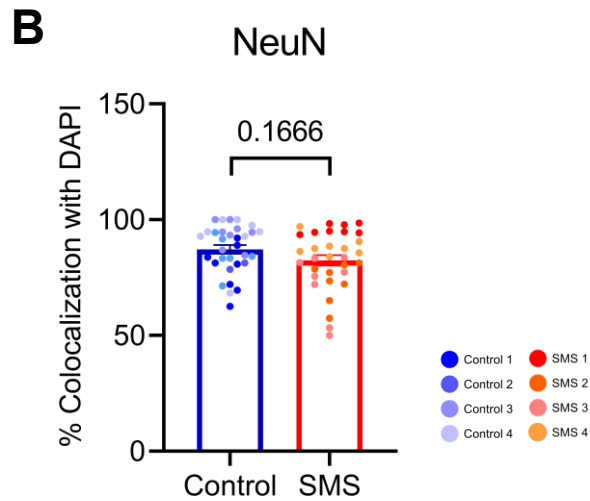
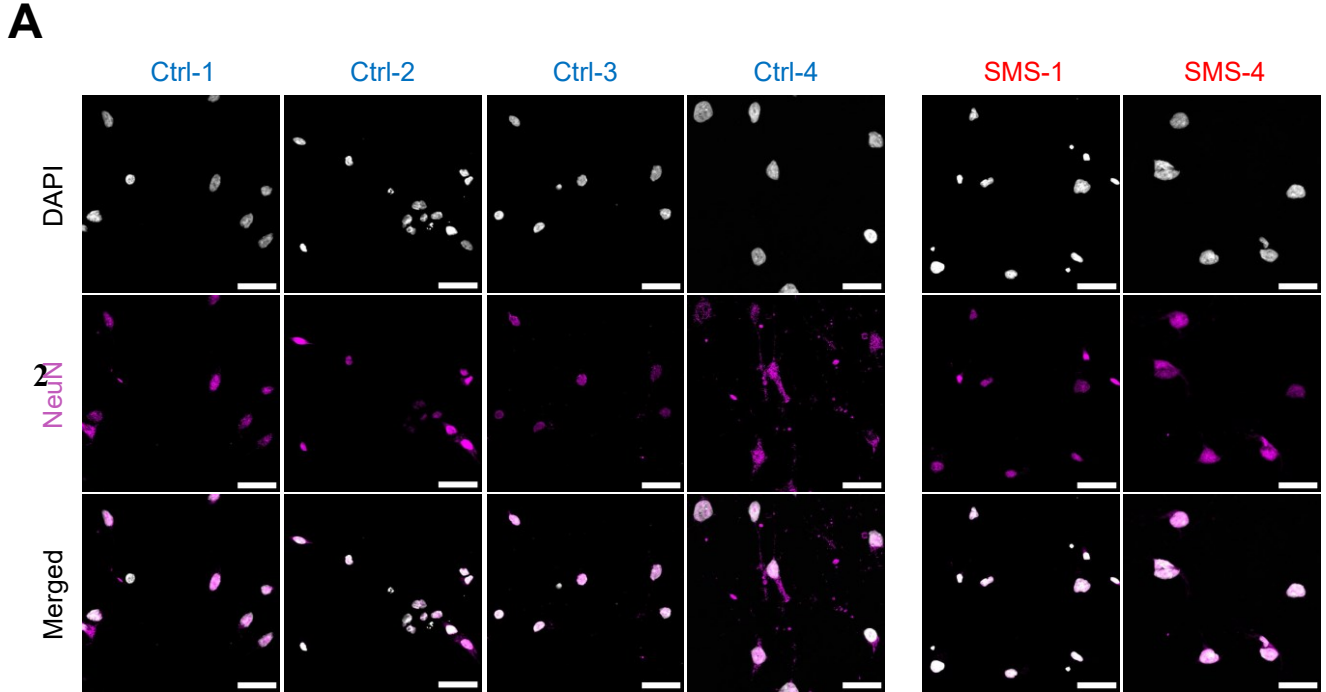


Figure 5. NeuN expression in hiPSC-derived forebrain neurons at 6 WPD.

A. Immunofluorescence staining of control and SMS hiPSC-derived forebrain neurons stained with DAPI (grey) and NeuN (magenta). (Scale bar: 20 μ m).

B. Quantification of control and SMS hiPSC-derived forebrain neurons expressing NeuN. (n = 32 images per condition, each point represents 1 image coloured based on genotype.)

Data presented as means \pm S.E.M.; p value by Mann Whitney test.

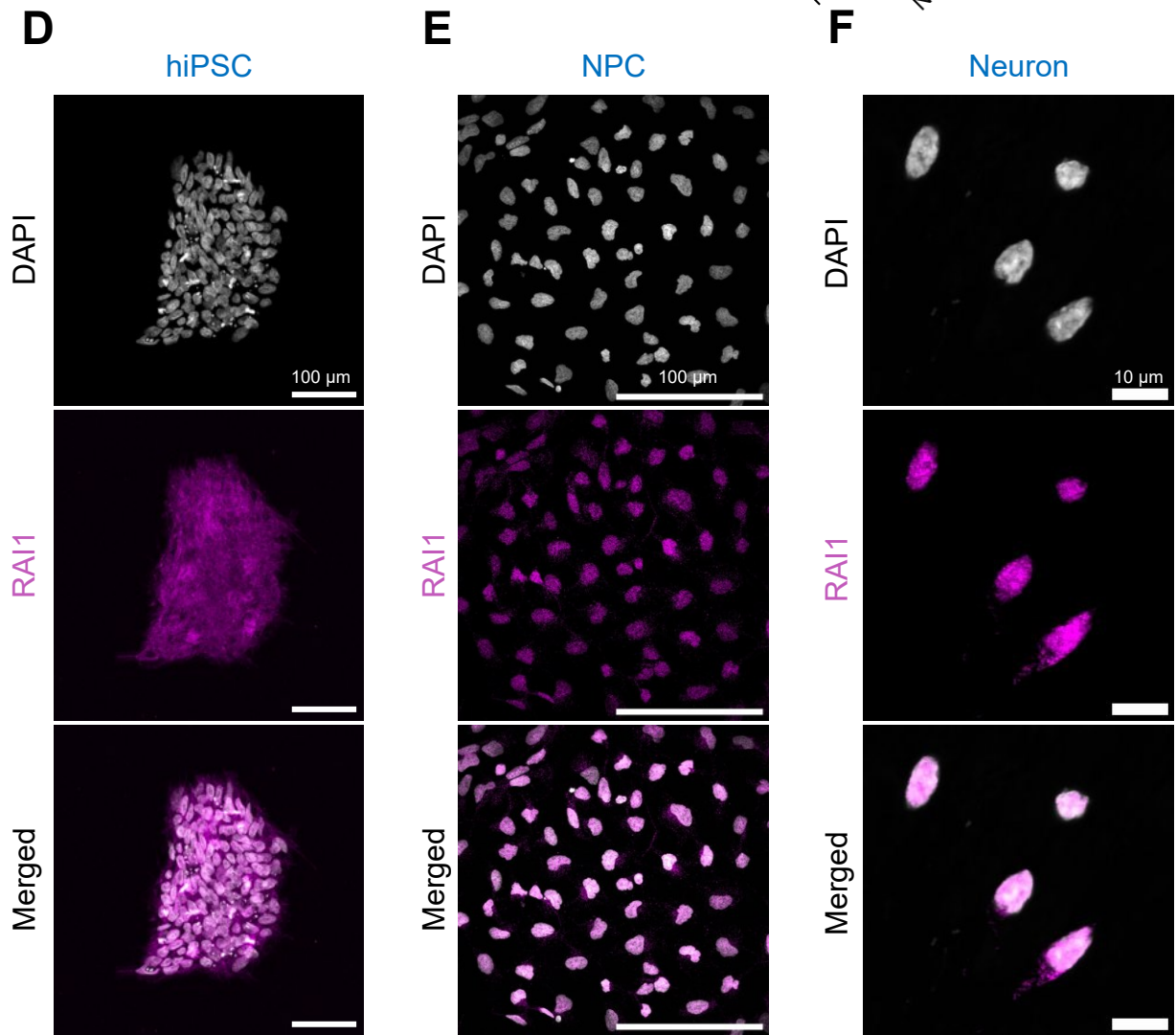
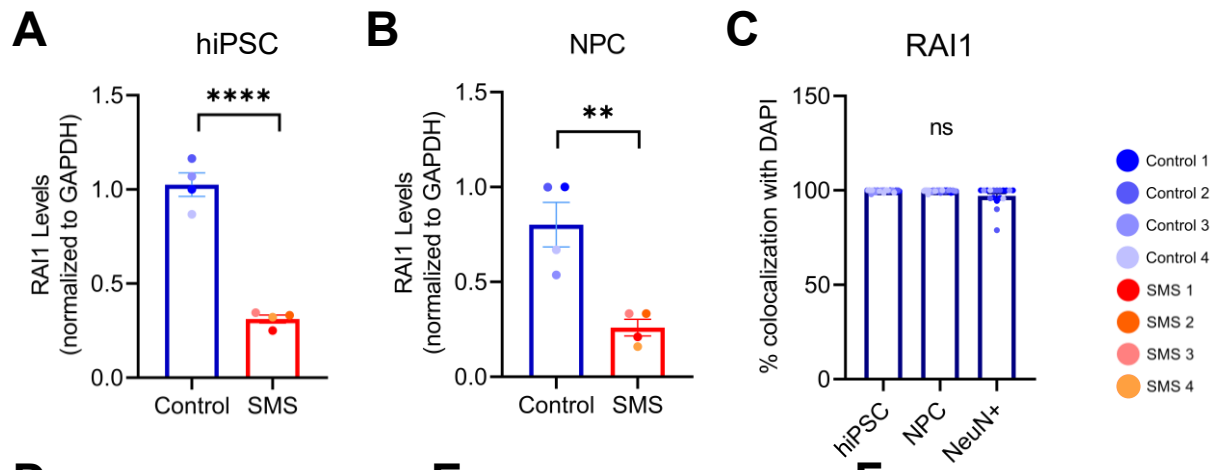


Figure 6. RAI1 expression in hiPSCs, NPCs, and neurons.

A. mRNA expression level of RAI1 in control and SMS hiPSCs assessed by qRT-PCR, normalized to housekeeping gene GAPDH. RAI1 is decreased in SMS hiPSCs (Each point represents the average of 3 technical replicates per line coloured based on genotype.) (-0.7129 ± 0.06583)

B. mRNA expression level of RAI1 is decreased in SMS hiPSC-derived NPCs compared to controls (Each point represents the average of 3 technical replicates per line coloured based on genotype.) (-0.5422 ± 0.1255)

Data presented as difference between means (SMS - Control) \pm S.D.; p value by unpaired t-test.

C. Quantification of control hiPSCs, NPCs, and NeuN+ neurons (6 WPD) expressing RAI1 based on immunostaining (n = 16 images per condition, each point represents 1 image coloured based on genotype.) Data presented as difference between means \pm S.E.M.; p value by Mann Whitney test.

D. Representative image of control hiPSCs immunostained for DAPI (grey) and RAI1 (magenta).

E. Representative image of control hiPSCs-derived NPCs immunostained for DAPI (grey) and RAI1 (magenta).

F. Representative image of control hiPSC-derived forebrain neurons at 6 WPD immunostained for DAPI (grey) and RAI1 (magenta). (Respective scale bars are noted).

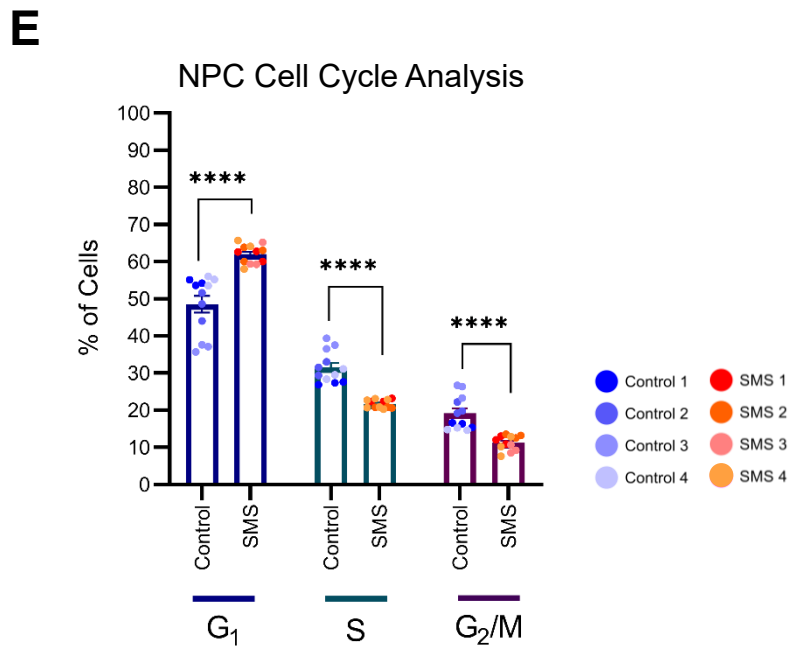
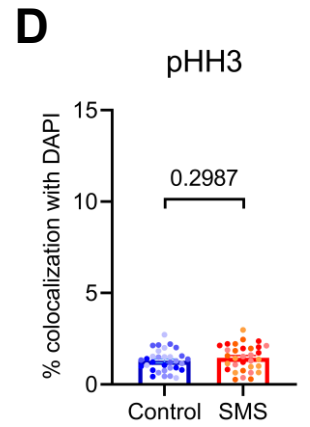
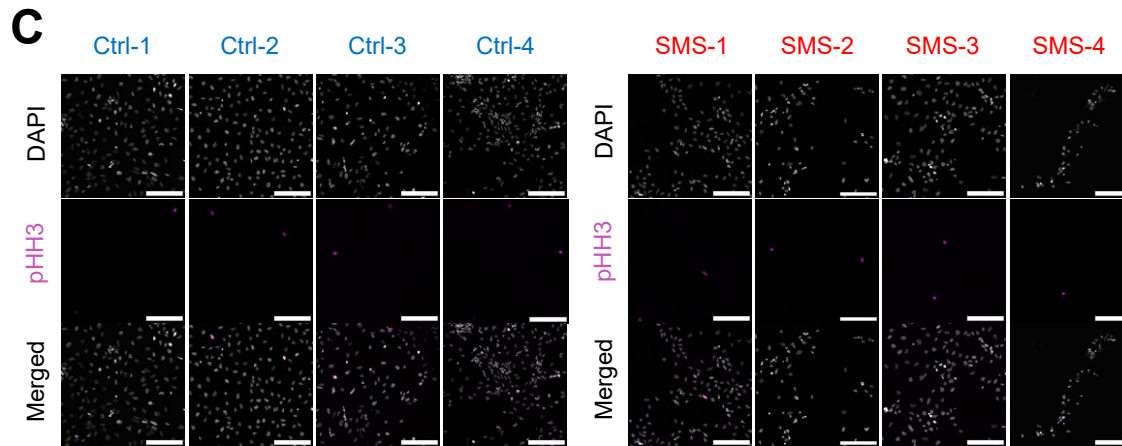
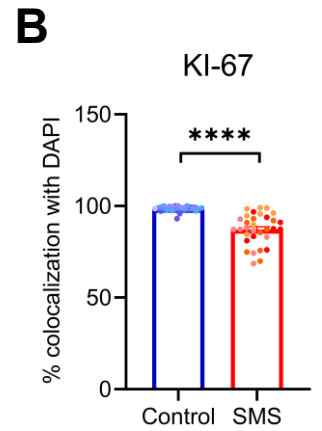
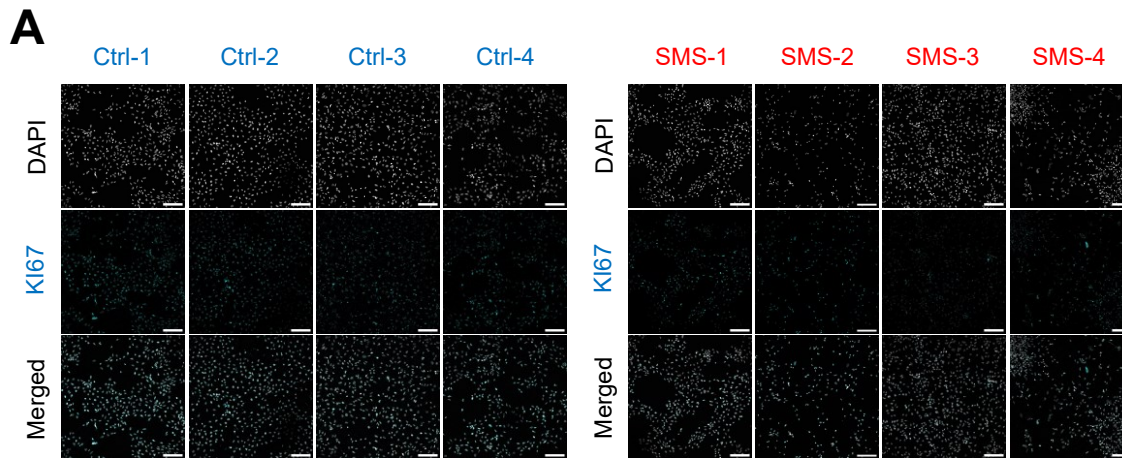


Figure 7. Altered cell cycle dynamics in SMS hiPSC-derived NPCs.

A. Immunofluorescence staining in control and SMS hiPSC-derived NPCs with antibodies for DAPI (grey) and KI67 (cyan). (Scale bar: 100 μ m).

B. Quantification of control and SMS NPCs expressing KI67 (n = 32 images per condition, each point represents 1 image, coloured based on genotype.) (-11.31 \pm 1.503).

C. Immunofluorescence staining in control and SMS hiPSC-derived NPCs with antibodies for DAPI (grey) and pHH3 (magenta). (Scale bar: 100 μ m).

D. Quantification of control and SMS NPCs expressing pHH3 (n = 32 images per condition, each point represents 1 image, coloured based on genotype.)

Data presented as difference between means (SMS - Control) \pm S.E.M.; p value by Mann Whitney test.

E. Bar plot of cell cycle analysis showing the percentage of hiPSC-derived control and SMS NPCs in G1, S, and G2/M phases, classified using the Watson pragmatic curve fitting algorithm.

In SMS NPCs samples, the percentage of cells in the G1 phase is increased (55.26 \pm 1.256), decreased in the S phase (-26.63 \pm 0.6135), and decreased in the G2/M phase (-15.21 \pm 0.6496).

(n = 3 biological replicates, each point represents one replicate colored based on genotype.

~17600-20000 cells per sample.) Data presented as discrepancy (SMS - Control) \pm S.E.M. of discrepancy; p value by one sample t-test.

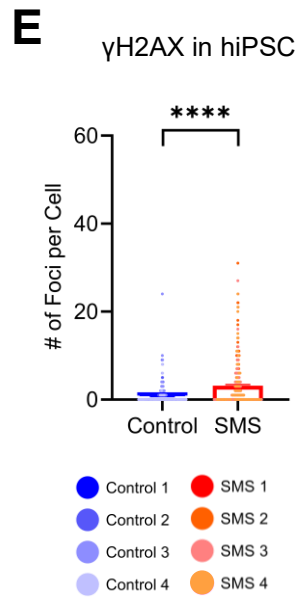
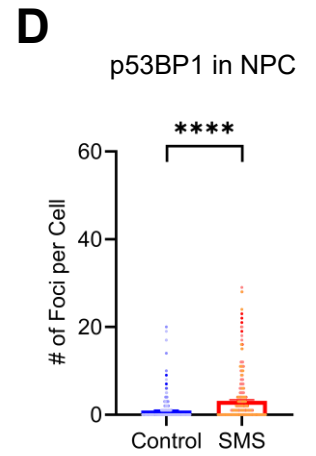
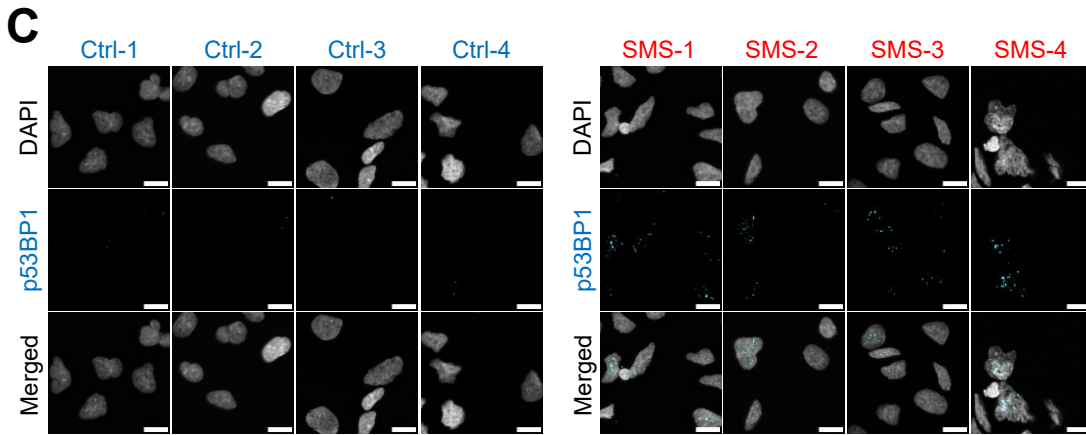
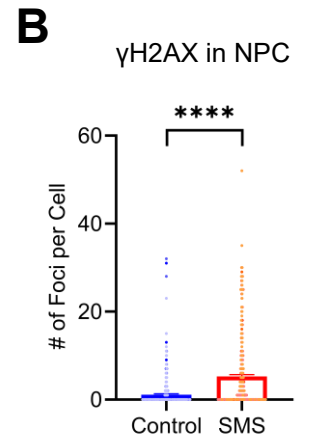
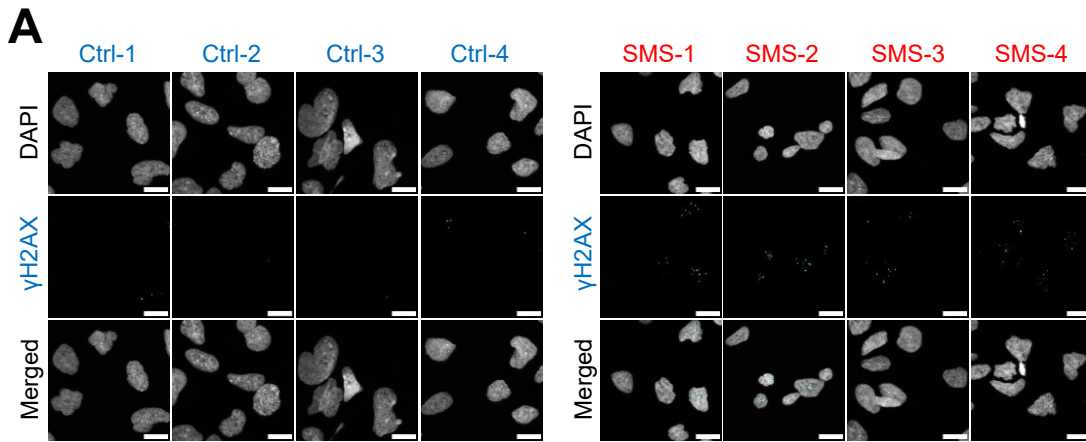


Figure 8. Increased DNA damage in SMS hiPSC-derived NPCs and hiPSCs.

A. Immunofluorescence staining in control and SMS hiPSC-derived NPCs with antibodies for DAPI (grey) and γ H2AX (cyan). (Scale bar: 10 μ m).

B. Quantification of immunostaining showing that SMS NPCs have a significantly greater number of γ H2AX foci per cell compared to controls (n = 400 cells per condition including n = 100 cells per genotype, each point represents one cell coloured based on genotype.) (4.115 ± 0.4539).

C. Immunofluorescence staining in control and SMS hiPSC-derived NPCs with antibodies for DAPI (grey) and p53BP1 (cyan). (Scale bar: 10 μ m).

D. Quantification of immunostaining showing that SMS NPCs have a significantly greater number of p53BP1 foci per cell compared to controls (n = 400 cells per condition including n = 100 cells per genotype, each point represents one cell coloured based on genotype.) (2.210 ± 0.2775).

E. Quantification of immunostaining showing that SMS hiPSCs have a significantly greater number of γ H2AX foci per cell compared to controls (n = 400 cells per condition including n = 100 cells per genotype, each point represents one cell coloured based on genotype.) (2.380 ± 0.2803).

Data presented as difference between means (SMS - Control) \pm S.E.M.; p value by unpaired t-test.

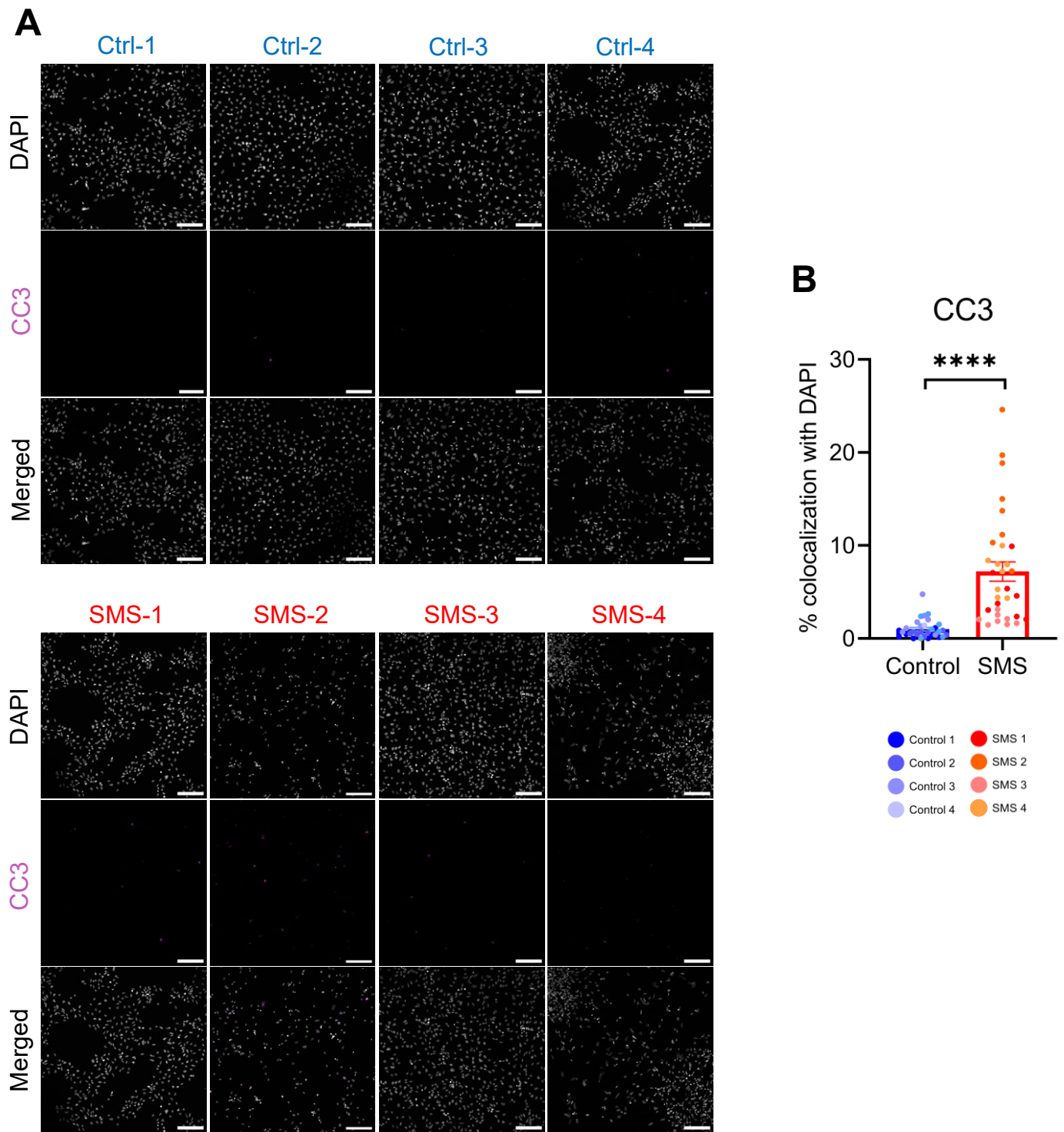


Figure 9. Increased apoptosis in SMS hiPSC-derived NPCs.

A. Immunofluorescence staining of control and SMS hiPSC-derived NPCs stained with DAPI (grey) and CC3 (magenta). (Scale bar: 100 μ m).

B. Quantification of control and SMS hiPSC-derived NPCs expressing CC3. SMS NPCs have a greater proportion of cells undergoing apoptosis compared to controls (n = 32 images per condition, each point represents 1 image, coloured based on genotype.) (6.210 ± 1.052)
Data presented as difference between means (SMS - Control) \pm S.E.M.; p value by Mann Whitney test.

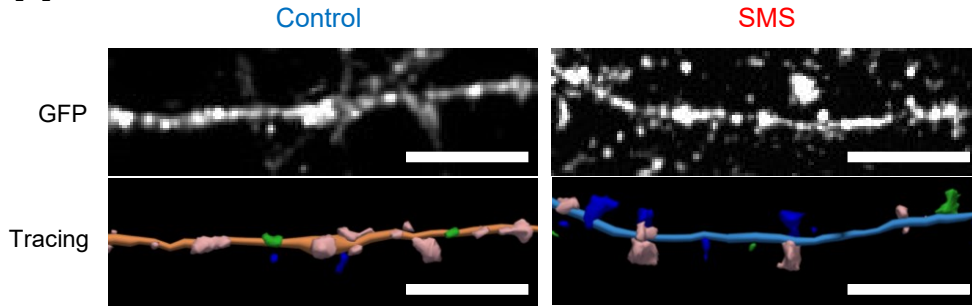
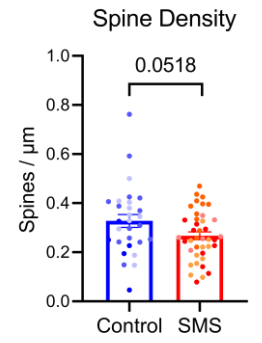
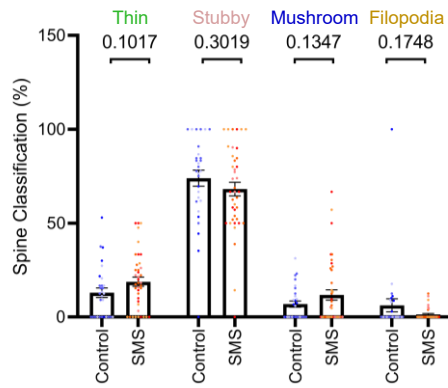
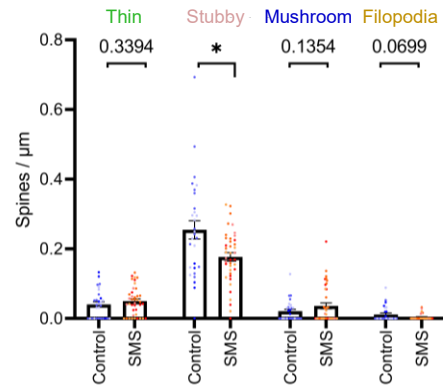
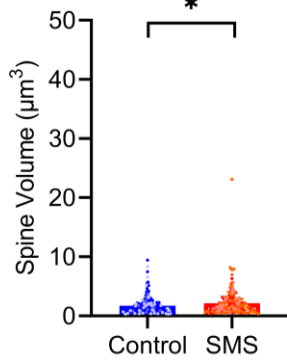
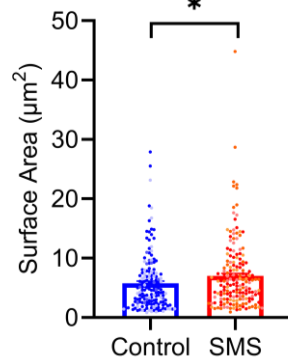
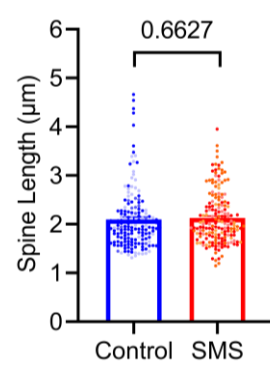
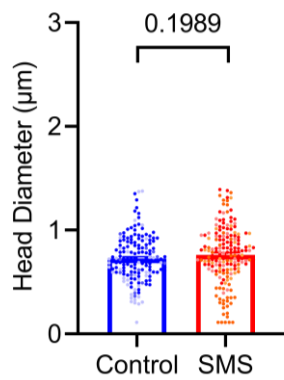
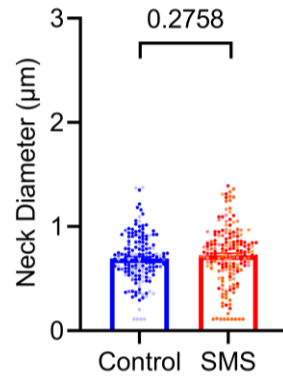
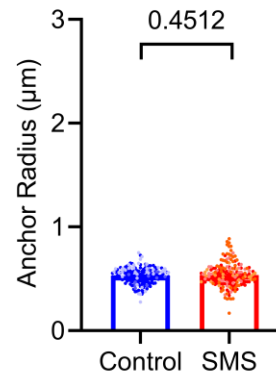
A**B****C****D****E****F****G****H****I****J**

Figure 10. Altered spine morphology in SMS hiPSC-derived neurons.

- A. Representative myr-GFP-transduced control and SMS hiPSC-derived neurons at 8 WPD, with corresponding 3D reconstructions. Four categories of spines labelled as: Thin - Green; Stubby - Pink; Mushroom - Blue; Filopodia - Yellow. Spine morphological parameters were quantified using the Neurolucida 360 software as described in Materials and Methods. (Scale bar: 10 μ m)
- B. Quantification of spine density in control and SMS hiPSC-derived neurons at 8 WPD (n = 29 tracings for controls, n = 40 tracings for SMS. Each point represents 1 tracing, coloured based on genotype.)
- C. Morphological classification of spines presented as percentage of spine type in control and SMS hiPSC-derived neurons (n = 29 tracings for controls, n = 40 tracings for SMS. Each point represents 1 tracing, coloured based on genotype.)
- D. Morphological classification of spines presented as density (spine type/ μ m) in control and SMS hiPSC-derived neurons. The density of stubby spines is decreased in SMS neurons compared to controls (-0.07786 ± 0.02884). (n = 29 tracings for controls, n = 40 tracings for SMS. Each point represents 1 tracing, coloured based on genotype.) Data presented as difference in means (SMS - Control) \pm S.E.M.; p value by unpaired t test with Welch's correction.
- E. Quantification of spine volume in control and SMS hiPSC-derived neurons. The mean spine volume is greater in SMS neurons compared to controls (n = 407 spines for controls, n = 477 spines for SMS. Each point represents 1 spine, coloured based on genotype.) (0.4233 ± 0.2048).
- F. Quantification of spine surface area in control and SMS hiPSC-derived neurons. The mean surface area is greater in SMS neurons compared to controls (n = 407 spines for controls, n = 477 spines for SMS. Each point represents 1 spine, coloured based on genotype.) (1.257 ± 0.5615).
- G. Quantification of spine length (n = 407 spines for controls, n = 477 spines for SMS. Each point represents 1 spine, coloured based on genotype.);
- H. Spine head diameter (n = 407 spines for controls, n = 477 spines for SMS. Each point represents 1 spine, coloured based on genotype.);
- I. Spine neck diameter (n = 407 spines for controls, n = 477 spines for SMS. Each point represents 1 spine, coloured based on genotype.);
- J. and Radius of spine anchor in control and SMS hiPSC-derived neurons (n = 407 spines for controls, n = 477 spines for SMS. Each point represents 1 spine, coloured based on genotype.) Data presented as difference in means (SMS - Control) \pm S.E.M.; p value by unpaired t test with Welch's correction.

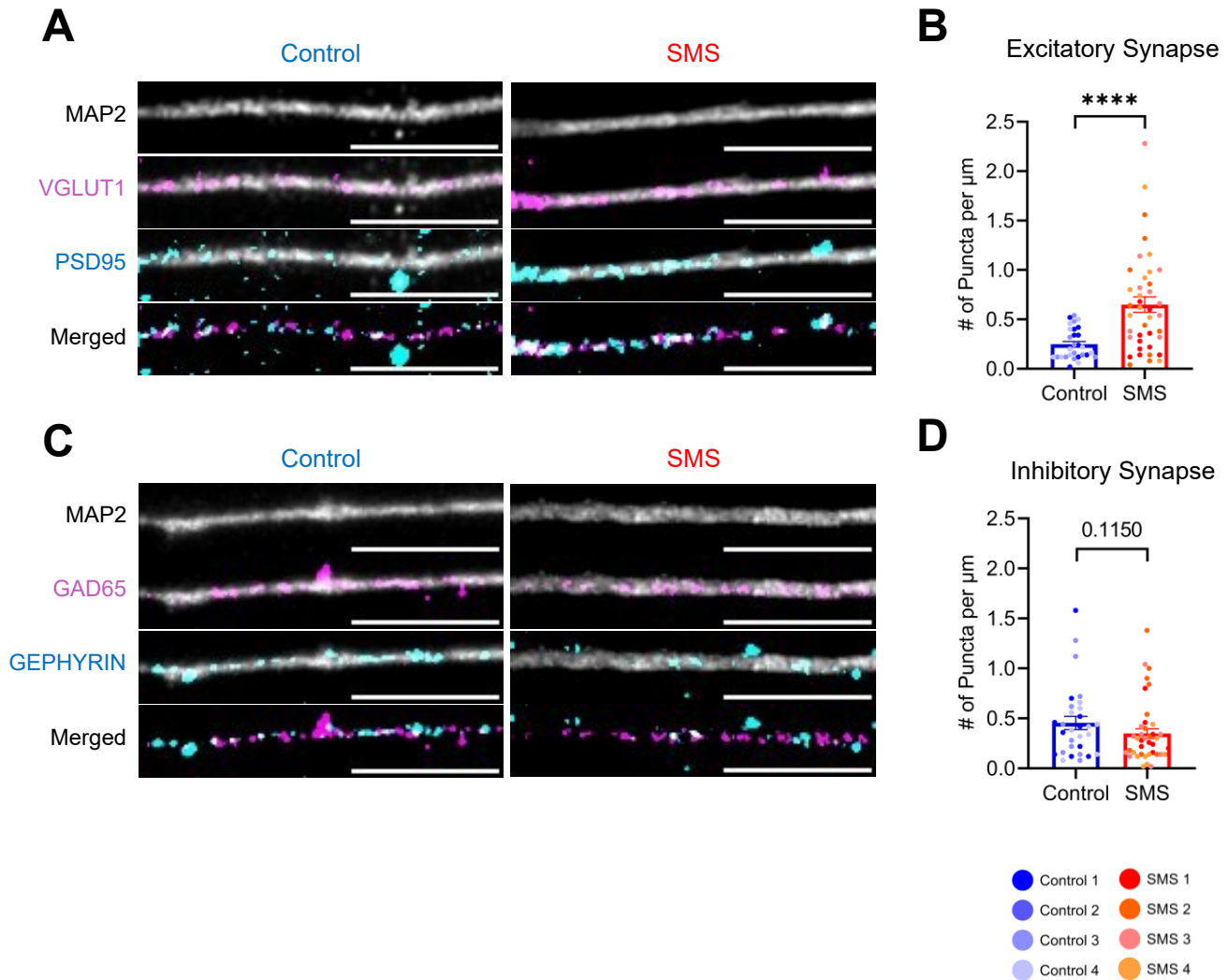


Figure 11. Increased excitatory synapse formation in SMS hiPSC-derived neurons.

A. Representative images of control and SMS hiPSC-derived neurons immunostained with MAP2 (grey), VGLUT1 (magenta), and PSD95 (cyan) (Scale bar: $10\mu\text{m}$).

B. Quantification of synaptic puncta with colocalized expression of VGLUT1 and PSD95 in control and SMS hiPSC-derived neurons. SMS neurons have increased functional excitatory synapses per μm compared to controls ($n = 40 \times 50\mu\text{m}$ neurite segments per condition, each point represents one $50\mu\text{m}$ segment, coloured based on genotype.) (0.4008 ± 0.09410).

C. Representative images of control and SMS hiPSC-derived neurons stained with MAP2 (grey), GAD65 (magenta), and GEPHYRIN (cyan) (Scale bar: $10\mu\text{m}$).

D. Quantification of synaptic puncta with colocalized expression of GAD65 and GEPHYRIN in control and SMS hiPSC-derived neurons. ($n = 40 \times 50\mu\text{m}$ neurite segments per condition, each point represents one $50\mu\text{m}$ segment, coloured based on genotype.)

Data presented as difference between means (SMS - Control) \pm S.E.M.; p value by Mann Whitney test.

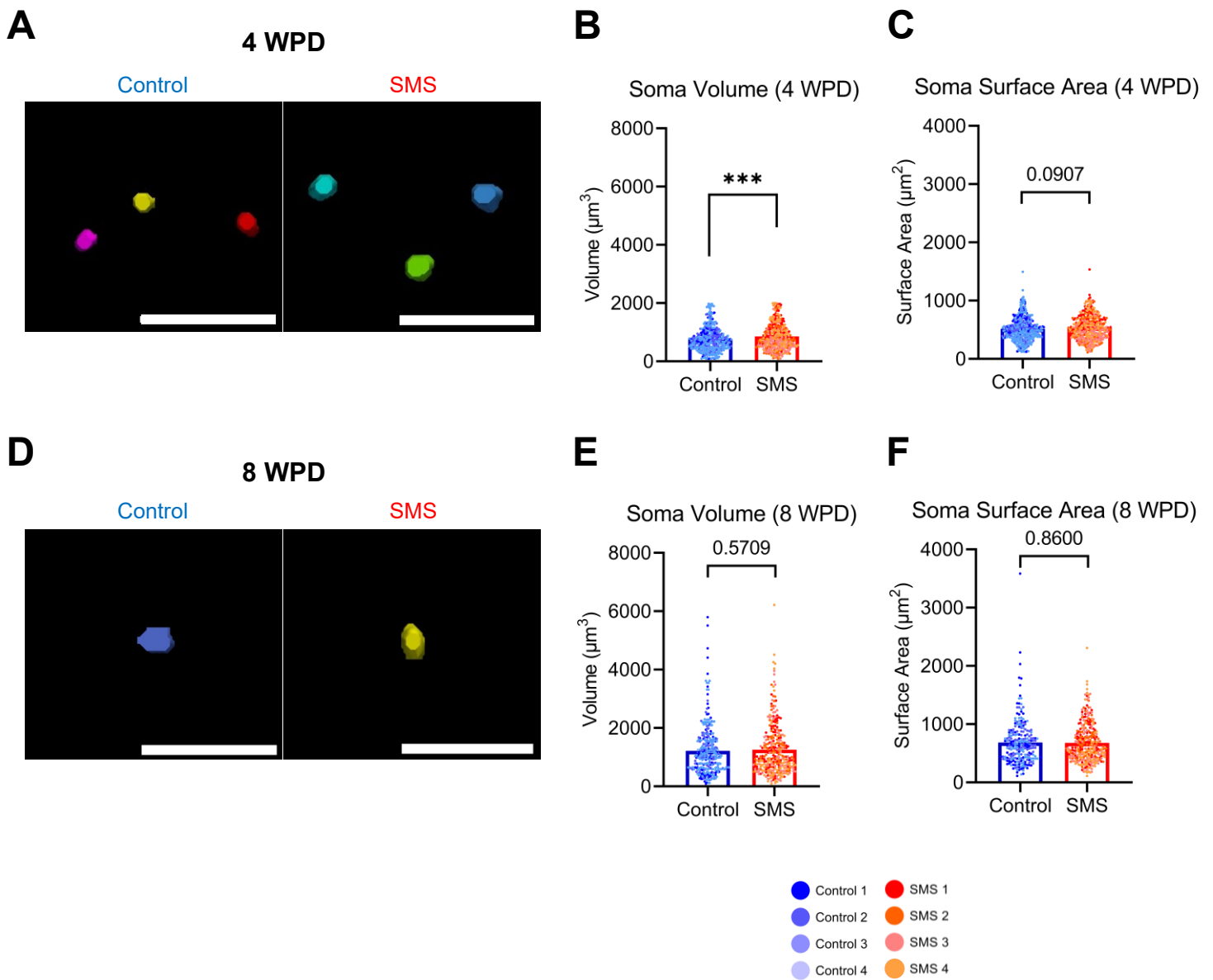


Figure 12. Soma morphological defects in SMS hiPSC-derived neurons.

A. Representative 3D tracings of myr-GFP-transduced control and SMS hiPSC-derived neurons' somas at 4 WPD (Scale bar: $50\mu\text{m}$).

B. Average soma volume of hiPSC-derived neurons at 4 WPD. SMS neurons at this timepoint have a greater average soma volume compared to controls ($n = 400$ cells per condition including 100 cells per genotype, each point represents 1 soma coloured based on genotype) (103.5 ± 30.34).

C. Average soma surface area of of hiPSC-derived neurons at 4 WPD ($n = 400$ cells per condition including 100 cells per genotype, each point represents 1 soma coloured based on genotype).

D. Representative 3D tracings of myr-GFP-transduced control and SMS hiPSC-derived neurons' somas at 8 WPD (Scale bar: 50 μ m).

E. Average soma volume of hiPSC-derived neurons at 8 WPD. (n = 300 cells per condition including 75 cells per genotype, each point represents 1 soma coloured based on genotype)

F. Average soma surface area of of hiPSC-derived neurons at 8 WPD. (n = 300 cells per condition including 75 cells per genotype, each point represents 1 soma coloured based on genotype)

Data presented as difference in means (SMS - Control) \pm S.E.M.; p value by unpaired t-test.

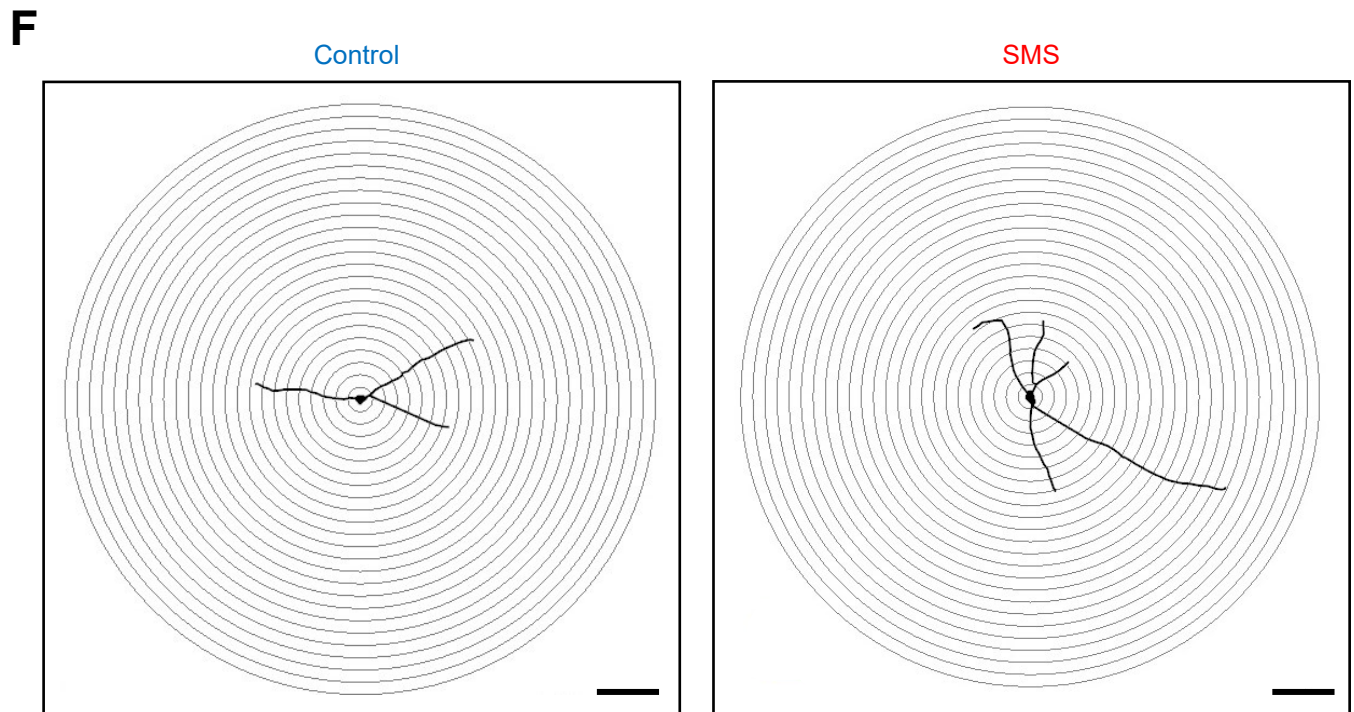
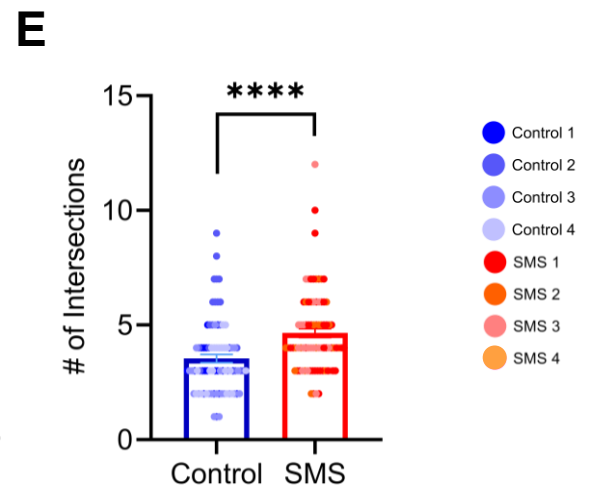
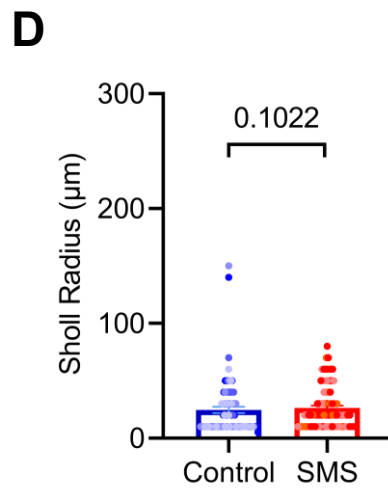
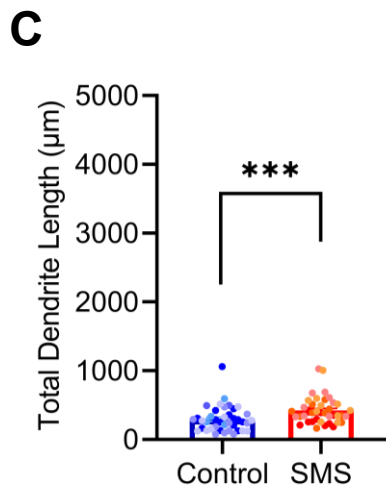
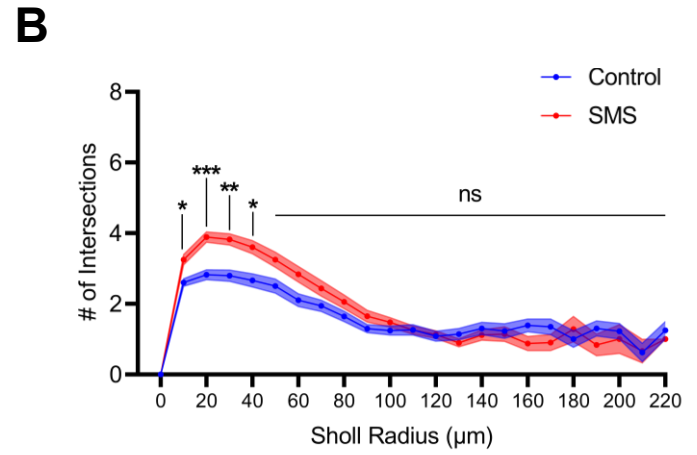
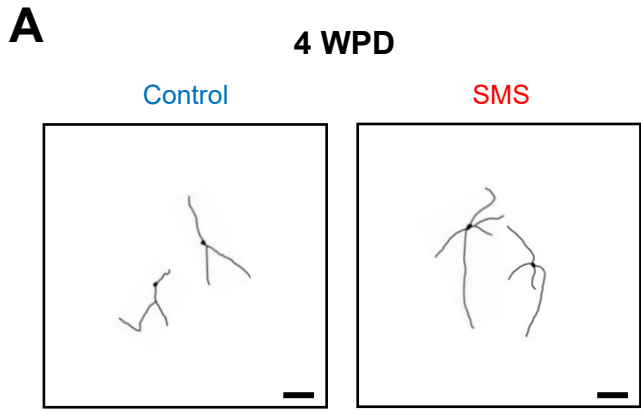


Figure 13. Sholl analyses of hiPSC-derived neurons at 4 WPD.

A. Representative 3D tracings of myr-GFP-transduced control and SMS hiPSC-derived neurons at 4 WPD. (Scale bar: 50 μ m).

B. Sholl analysis of control and SMS hiPSC-derived neurons at 4 WPD. SMS neurons have increased dendrite complexity compared to controls at 10, 20, 30, and 40 μ m from the soma (n = 80 neurons per condition including 20 neurons per genotype, each point represents 1 neuron coloured based on genotype). (10 μ m: $0.6500 \pm 0.0.1850$; 20 μ m: 1.063 ± 0.2042 ; 30 μ m: 1.025 ± 0.2327 ; 40 μ m: 0.9375 ± 0.2666 , presented as differences between means \pm S.E. of difference). p values by multiple t-tests.

C. Quantification of total dendrite length of myr-GFP⁺ neurons from control and SMS hiPSC-derived neurons at 4 WPD. SMS neurons at this timepoint have a greater average total dendrite length compared to controls (n = 40 neurons per condition including 10 neurons per genotype, each point represents 1 neuron coloured based on genotype). (128.2 ± 42.26 , presented as difference between means \pm S.E.M.).

D. Quantification of Sholl critical radius of control and SMS hiPSC-derived neurons at 4 WPD (n = 80 neurons per condition including 20 neurons per genotype, each point represents 1 neuron coloured based on genotype).

E. Quantification of maximum crossings at Sholl critical radius of control and SMS hiPSC-derived neurons at 4 WPD. SMS neurons at this timepoint have a greater average number of intersections at critical radii compared to controls (n = 80 neurons per condition including 20 neurons per genotype, each point represents 1 neuron coloured based on genotype). (1.113 ± 0.2675 , presented as difference between means (SMS - Control) \pm S.E.M.).

F. Representative tracings with Sholl radii of control and SMS hiPSC-derived neurons at 4 WPD. (Scale bar: 50 μ m).

p values by Mann Whitney test unless otherwise indicated.

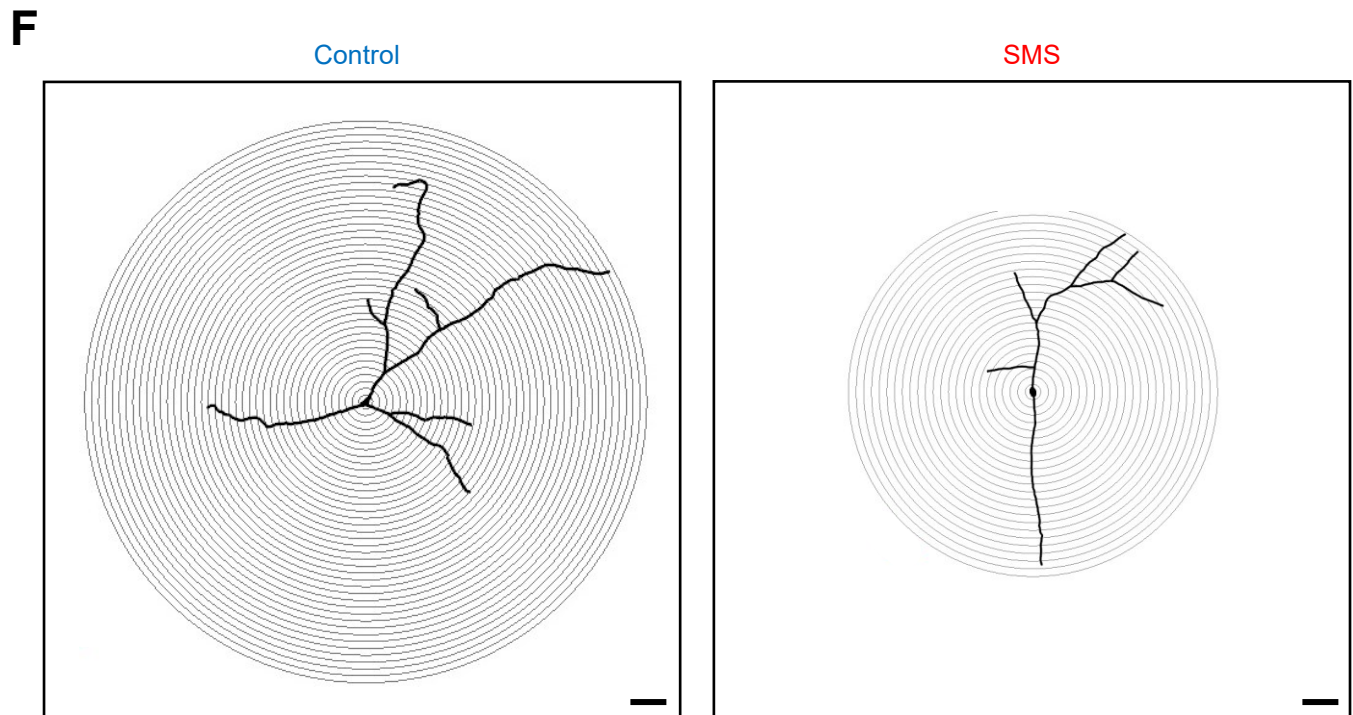
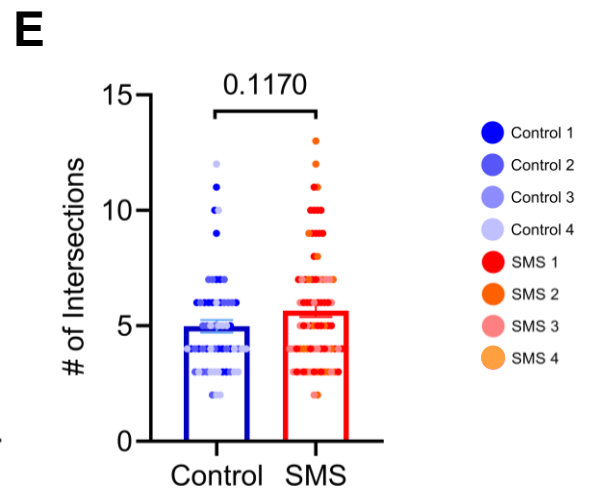
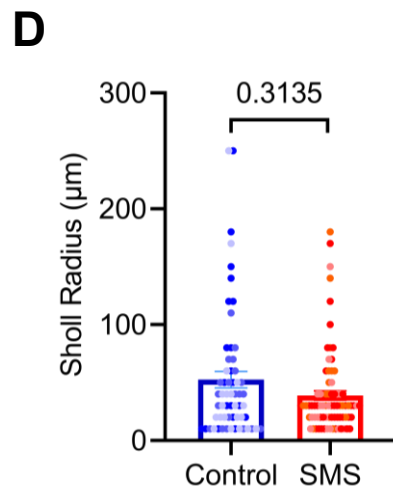
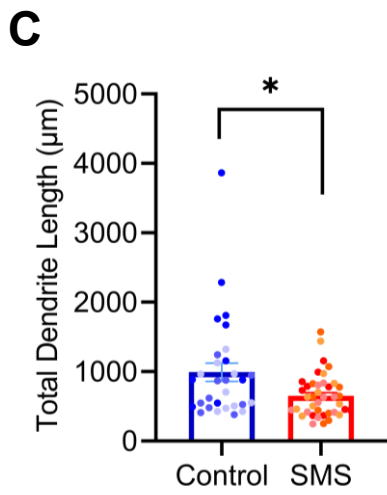
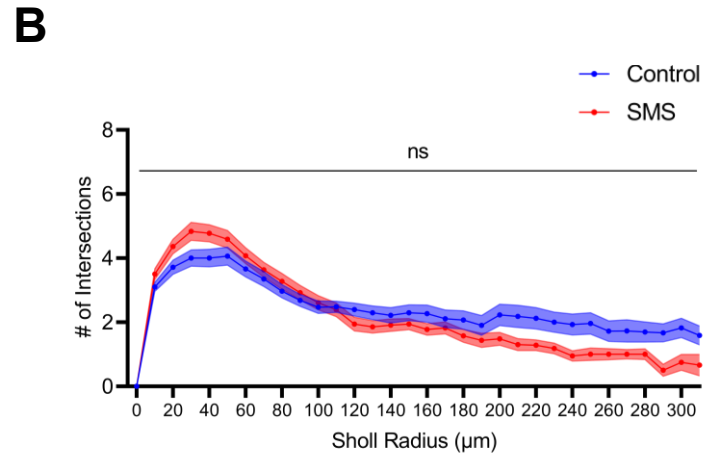
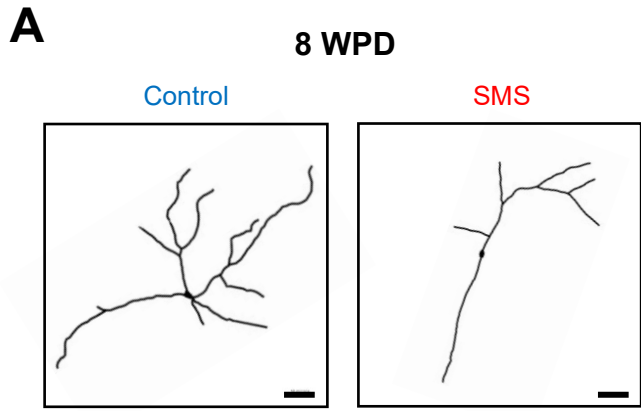


Figure 14. Sholl analyses of hiPSC-derived neurons at 8 WPD.

A. Representative 3D tracings of myr-GFP-transduced control and SMS hiPSC-derived neurons at 8 WPD. (Scale bar: 50 μ m).

B. Sholl analysis of control and SMS hiPSC-derived neurons at 8 WPD. (n = 60 neurons for controls, n= 80 neurons for SMS including 20 neurons per genotype, each point represents 1 neuron coloured based on genotype). Data presented as differences between means \pm S.E. of difference). Statistical analysis by multiple t-tests.

C. Quantification of total dendrite length of myr-GFP+ neurons from control and SMS hiPSC-derived neurons at 8 WPD. SMS neurons at this timepoint have a lower total dendrite length compared to controls (n = 40 neurons for controls, n= 30 neurons for SMS including 10 neurons per genotype, each point represents 1 neuron coloured based on genotype). (-340.9 \pm 127.5, presented as difference between means \pm S.E.M.).

D. Quantification of Sholl critical radius of control and SMS hiPSC-derived neurons at 8 WPD. (n = 60 neurons for controls, n= 80 neurons for SMS including 20 neurons per genotype, each point represents 1 neuron coloured based on genotype).

E. Quantification of maximum crossings at Sholl critical radius of control and SMS hiPSC-derived neurons at 8 WPD. (n = 60 neurons for controls, n= 80 neurons for SMS including 20 neurons per genotype, each point represents 1 neuron coloured based on genotype).

F. Representative tracings with Sholl radii of control and SMS hiPSC-derived neurons at 8 WPD. (Scale bar: 50 μ m).

p values by Mann Whitney test unless otherwise indicated.